CALPHAD: Computer Coupling of Phase Diagrams and Thermochemistry 68 (2020) 101722

Contents lists available at ScienceDirect

Calphad

journal homepage: http://www.elsevier.com/locate/calphad

An evaluation of the Mn–Ga system: Phase diagram, crystal structure, magnetism, and thermodynamic properties

Liangyan Hao, Wei Xiong *

Physical Metallurgy and Materials Design Laboratory, Department of Mechanical Engineering and Materials Science, University of Pittsburgh, Pittsburgh, USA

ARTICLE INFO

Keywords:
Ga–Mn
Phase equilibria
Magnetocaloric
Magnetic transition
Heusler compound

ABSTRACT

The Ni–Mn-Ga alloy system is attractive due to its functional properties with potentials in various applications. However, the fundamental alloy thermodynamics of the binary Mn–Ga system is still lack of investigation. Therefore, a comprehensive evaluation of the Mn–Ga is performed in this work. Different versions of Mn–Ga phase diagrams available in the literature are reviewed. A new version of the Mn–Ga phase diagram is recommended along with possible invariant reactions. The crystal structure, magnetic transition, and thermochemical properties of intermetallic compounds are reviewed by considering available experimental and modeling such as ab initio calculations. In fact, more experimental information on the Mn-rich side is required in order to perform CALPHAD thermodynamic modeling for a reliable database. Further experiments are recommended to study the high-temperature phase equilibria between liquid, (γMn), (δMn) and Mn_2Ga(h), phase reactions between Mn_8Ga_5 and Mn_7Ga_6, and invariant reactions involving the MnGa phase. Nevertheless, the summarized information on phase equilibria, phase diagram, crystallography, magnetic transition temperature, magnetic moment, heat capacity, and enthalpy of formation can support the future thermodynamic investigation of the Mn–Ga system, which is critical for the materials design and discovery of Ni–Mn-Ga alloys.

1. Introduction

In recent years, Mn-Ga-based Heusler compounds such as Ni_2MnGa have received attention due to their magnetic- or thermo-induced martensitic transformation and giant magnetocaloric effects. Hence, they find applications in actuators [1,2] and refrigerants [3,4]. Epitaxial growth of ferromagnetic Mn–Ga thin films on semiconductor substrates such as GaAs and GaN has been applied for the fabrication of novel magneto-electronic and magneto-optical devices [5–7]. Several intermetallic compounds in the Mn–Ga system can be a potential candidate for different applications. For example, antiferromagnetic $D0_{19}$-type Mn_3Ga can be used in the exchange bias of magneto-resistive components, such as spin valve and magnetic tunnel junction [8,9]. Ferrimagnetic $D0_{22}$-type Mn_3Ga and ferromagnetic $L1_0$-type MnGa exhibit high Curie temperature, spin polarization, coercivity, and magnetic anisotropy, so they are promising materials for rare-earth-free hard magnets [10–12] and spintronic devices [13–15].

An important feature of the Mn–Ga intermetallic compounds is that their magnetic properties can be easily altered by varying the alloy composition and processing. Therefore, knowledge of the phase equilibria, crystallography, and thermodynamic properties is crucial for Mn-Ga-based functional materials design. However, the essential information, such as the phase equilibria, available in the literature [16–19], varies significantly from each other. The first thermodynamic modeling for the Mn–Ga system was performed by Sedmidubský *et al* [20]. The main focus of their work is on the modeling of the ternary Ga-Mn-N system, and hence, the assessment of the binary Mn–Ga system was over-simplified and cannot reproduce the phase equilibria and thermodynamic properties of the Mn–Ga system accurately. The liquid phase was treated as an ideal solution, all intermetallic compounds were modeled as stoichiometric compounds, and there is no solubility limit of Ga in (αMn) considered in the modeling. The solubility limit of Ga in the other three Mn allotropes are also over-simplified with simple models. For example, both (γMn) and (δMn) are modeled as the ideal solution only.

Therefore, for the sake of materials design with the Mn–Ga system involved, a reliable thermodynamic description of the Mn–Ga system is highly in desire. In this work, the phase equilibria, crystallographic

* Corresponding author. 3700 O'Hara St., Pittsburgh, PA, 15261, USA.
E-mail addresses: weixiong@pitt.edu, w-xiong@outlook.com (W. Xiong).
URL: http://www.pitt.edu/~weixiong (W. Xiong).

https://doi.org/10.1016/j.calphad.2019.101722
Received 20 October 2019; Received in revised form 9 December 2019; Accepted 11 December 2019
Available online 30 December 2019
0364-5916/

information, magnetic and thermochemical properties of the Mn–Ga system are critically evaluated. A new version of the Mn–Ga phase diagram is recommended based on such a comprehensive review. This comprehensive review will serve as the basis for the improved thermodynamic modeling of the Mn–Ga system.

2. Phase equilibria

The Mn–Ga phase diagram is complicated due to the presence of a variety of intermetallic compounds, among which some exhibit magnetism. Besides, there are four allotropes of Mn, and the difference between the melting points of Mn and Ga is as high as 1216 °C. The low melting point (29.76 °C) of Ga and the high vapor pressure of Mn also impose difficulties on phase diagram determination. So far, systematic studies of the Mn–Ga phase diagram are quite limited, as listed in Table 1. And the reported experimental Mn–Ga phase diagrams shown in Fig. 1 are significantly different.

2.1. Experimental studies

The first systematic investigation of the Mn–Ga phase diagram over the whole composition range was performed by Meissner et al. [16] (Fig. 2) in 1965. Alloys less than 50 at.% Ga were melted in sintered corundum crucibles under argon (Ar) and cooled in the electric furnace. Other Ga-rich alloys were melted in encapsulated quartz tubes. Pure electrolytic Mn (99.8 wt.%) and high-grade Ga (99.99 wt.%) were used for sample preparation. Chemical analysis indicated that the weight loss of each alloy after melting is small. Before X-ray diffraction and thermal analysis, annealing was performed at different temperatures for different periods varying from 200 h at 300 °C to 5 h at 1000 °C. Since the diffusion information is even less than thermodynamics of the Mn–Ga system, it is difficult to evaluate how long for the annealing is sufficient enough to approach equilibrium. The same question applies to other reported phase diagram determinations of the Mn–Ga system.

Ten intermetallic compounds and thirteen invariant reactions were reported by Meissner et al. [16]. The two-phase region between the liquid and (γMn) is relatively wide, spanning from 990 to 1180 °C (Fig. 2(a)). The cubic (γMn) phase was reported to have a metastable tetragonal modification with $L1_0$ ordering in alloys with 10 to 20 at.% Ga quenched between 800 and 1000 °C. Polymorphic transformation within the Mn_8Ga_5 phase occurs between 770 and 860 °C (Fig. 2(b)). As the composition of Ga or temperature increases, the structure of the Mn_8Ga_5 phase distorts from cubic to rhombohedral. The crystal structure of Mn_5Ga_7 phase was not resolved, but a polymorphic transformation was detected at 545 °C based on both thermal and X-ray diffraction (XRD) analysis (Fig. 2(c)). As shown in Fig. 2(c), all Ga-rich intermetallic compounds were treated as the line compounds in this version. They all form from a peritectic reaction, except for the Mn_2Ga_5 phase, which forms through a peritectoid reaction. On the Mn-rich side, phase equilibria were not established clearly, and hence, phase boundaries were indicated as dashed lines. This version of the Mn–Ga phase diagram was adopted in the latest ASM handbook compiled by Okamoto [21].

In the same year 1965, Wachtel and Nier [17] determined the Mn–Ga phase diagram over the whole composition range based on the magnetic susceptibility measurement. Sample preparation was similar to Meissner et al. [16] by performing the melting of alloys in the sintered corundum inside of the encapsulated quartz tube filled with Ar. Although the purity of Ga (99.95 wt.%) for alloy preparation is similar to Meissner et al. [16] (99.99 wt.%), the purity of Mn (99.99 wt.%) as the raw material is higher than that of Meissner et al. [16] (99.8 wt.%). Before phase diagram determination, a multi-stage homogenization was carried out at a temperature just below the solidus, but never above 1000 °C. The magnetic susceptibility of different alloys was measured over a whole composition range in order to determine the phase transition temperature shown in the phase diagram (Fig. 3). Thirteen intermetallic compounds were identified, and their compositions were reported as the ideal stoichiometry. In this version [17], the liquid + (γMn) two-phase region is narrow, from 1000 to 1014 °C (Fig. 3(a)). A phase that forms from a peritectoid reaction between Mn_8Ga_5 and MnGa phases at 635 °C was not clearly stated (Fig. 3(b)). This unknown phase was also reported to react with the Mn_3Ga_2 phase to form the Mn_8Ga_5 phase. However, such a phase was not reported in others' work [16,18,19]. Eighteen invariant reactions were suggested in this version. Polymorphic transformations were detected for the $MnGa_3$ and $MnGa_6$ phases. All Ga-rich intermetallic compounds have a homogeneity range and they form via a peritectic reaction (Fig. 3(c)). The magnetic and electronic properties of the Mn–Ga solid phases were also studied in this work, but their crystal structures were not investigated.

Later in 1980, another version of the Mn–Ga phase diagram was suggested by Lu et al. [18], which included only five intermetallic compounds. Samples prepared from pure Mn (99.99 wt.%) and pure Ga (99.9 wt.%) were induction melted in Al_2O_3 crucibles. To reduce the evaporation of Mn, the Al_2O_3 crucibles were covered by graphite crucibles and filled with Ar. Besides, for each as-cast sample, the Mn composition was analyzed to check the weight loss, but the results were not reported. Homogenizations at 900 and 600 °C for 15 days were applied to Mn-rich (less than 30 at.% Ga) and Ga-rich (30–60 at.% Ga) alloys, respectively. Due to the low melting point, homogenization was not applied to the alloys higher than 60 at.% Ga. Followed by homogenization, the annealing for equilibrium alloys are applied at different temperature for 1–6 h, which may be an issue of this experimental work. Due to the insufficient annealing and long-term homogenization, it is challenging to identify the equilibrium state for each alloy at different temperatures, although authors choose the annealing temperature as the equilibrium temperature for phase diagram construction (Fig. 4).

In the work by Lu et al. [18], phase boundaries of (δMn) were tentatively determined. The most interesting feature of this phase diagram is the two-stage polymorphic transformation within the (γMn) phase. As the temperature decreases, the (γMn) phase transforms from disordered face-centered cubic phase γ_1 to disordered face-centered tetragonal phase γ_2 and then to face-centered tetragonal phase with $L1_0$ ordering γ_3 (Fig. 4(a)). Thus, the (γMn) phase exists within a wide temperature range (0–1133 °C) and γ_3 is stable down to room

Table 1
Available experimental investigations for the Mn–Ga phase diagram.

Temperature/Composition Range Studied	Experimental Technique	Ref.
0–1400 °C, 0 ~ 100 at.% Ga	XRD, DTA	[16]
100–1300 °C, 0 ~ 100 at.% Ga	Magnetic measurement	[17]
0–800 °C, 19.0 ~ 31.2 at.% Ga	XRD, thermal expansion and magnetic measurements	[23]
0–1300 °C, 0 ~ 100 at.% Ga	XRD, DTA, magnetic measurement	[18]
400–1400 °C, 0 ~ 45 at.% Ga	XRD, DSC, EPMA	[19]
0–600 °C, 75 ~ 100 at.% Ga	single crystal XRD, EDX, DTA	[24]

Abbreviations: XRD, X-ray diffraction; DTA, differential thermal analysis; DSC, differential scanning calorimetry; EPMA, electron probe micro-analyzer; EDX, energy dispersive X-ray analysis.

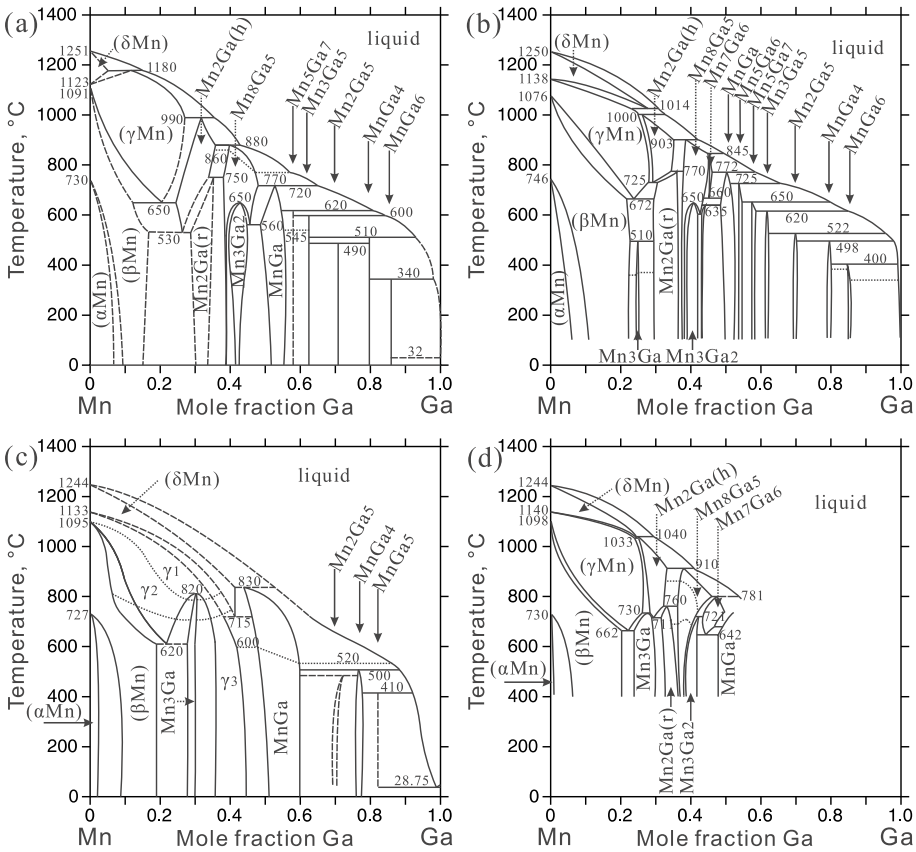

Fig. 1. Different versions of the Mn–Ga phase diagram based on the experimental results from: (a) Meissner et al. [16]; (b) Wachtel and Nier [17]; (c) Lu et al. [18]; (d) Minakuchi et al. [19]. The dashed lines represent unsettled phase boundaries. The dotted lines represent polymorphic transformations.

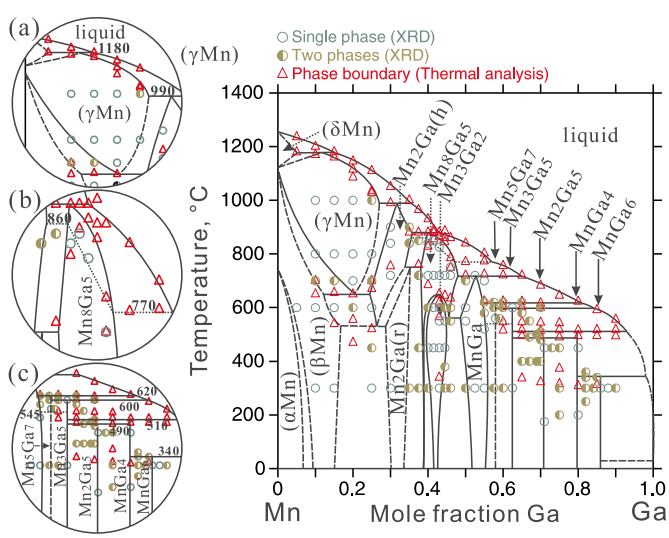

Fig. 2. The Mn–Ga phase diagram determined by Meissner et al. [16].

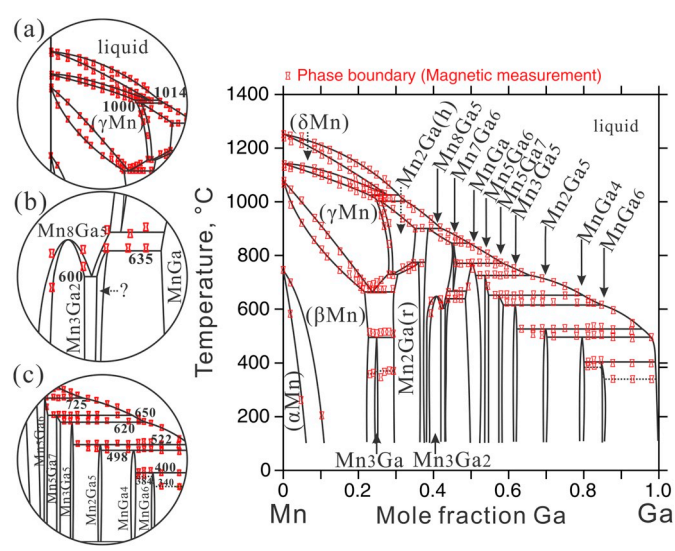

Fig. 3. The Mn–Ga phase diagram determined by Wachtel and Nier [17].

temperature with a homogeneity range of 36.1 to 43.7 at.% Ga, which essentially lies in the phase region of Mn_3Ga_2 according to the two previous versions [16,17]. Moreover, the liquid + (γMn) two-phase region and phase equilibria between the liquid, (δMn), and (γMn) phases were not investigated. Seven invariant reactions and a congruent transformation from γ_1 to Mn_3Ga at about 820 °C were reported. A polymorphic transition was detected to exist in the MnGa phase at 520–600 °C (Fig. 4(b)), but the crystal structure of this phase was not resolved due to complex XRD patterns. Only three Ga-rich phases were proposed, among which the crystal structure and homogeneity range of Mn_2Ga_5 and $MnGa_5$ phases were not determined (Fig. 4(c)). This version of the Mn–Ga phase diagram is questionable because it incorporates several phases in one region due to the complex XRD patterns. For example, the single-phase region for (δMn) spans from 715 to 1244 °C and from 0 to 42 at.% Ga, which contains the phase regions of $Mn_2Ga(h)$ and Mn_8Ga_5 in other versions [16,17,19]. This version was adopted in the previous ASM handbook compiled by Massalski and Okamoto [22].

Recently, the Mn-rich side of the Mn–Ga phase diagram was

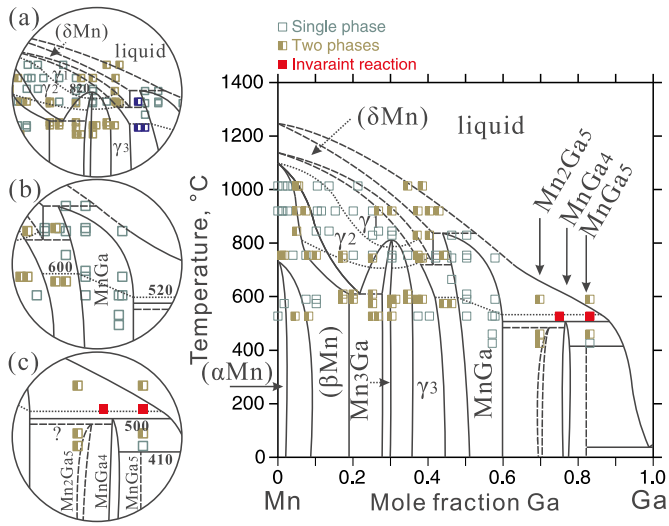

Fig. 4. The Mn–Ga phase diagram determined by Lu et al. [18].

reinvestigated by Minakuchi et al. [19] in 2012, with major emphasis on the stability range of Mn_3Ga phase and the high-temperature phase equilibria. 99.7 wt.% pure Mn and 99.999 wt.% pure Ga were used for alloy melting in an induction furnace under the Ar atmosphere. Each alloy was heat-treated in the encapsulated vacuum quartz tube with backfilled Ar. The annealing was performed properly at different temperatures for the periods ranging from 3 h (1000 °C) to 30 days (500 °C). However, the composition deviation of alloys was not reported by Minakuchi et al. [19].

The reported phases and phase equilibria are similar to those by Wachtel and Nier [17], but both Mn_3Ga and Mn_7Ga_6 phases have a wider homogeneity range and are stable over a wider temperature range. Furthermore, liquid + (γMn) two-phase region does not exist (Fig. 5(a)). A two-stage polymorphic transformation within the Mn_8Ga_5 phase was detected (Fig. 5(b)). Three structural variants (high--temperature, intermediate-temperature, and low-temperature) of Mn_8Ga_5 were reported. Due to the difficulty in obtaining a single phase high-temperature or intermediate-temperature Mn_8Ga_5, only the crystal structure of the low-temperature Mn_8Ga_5 phase was determined using the XRD analysis. This version did not include phase boundaries representing a structural change of the Mn_8Ga_5 phase in Mn_8Ga_5 + Mn_3Ga_2 and Mn_8Ga_5 + Mn_7Ga_6 two-phase regions. Based on the XRD results, both Mn_2Ga(h) and Mn_3Ga_2 phases have a face-centered tetragonal structure with $L1_0$ ordering and they are separated by the low-temperature Mn_8Ga_5 phase.

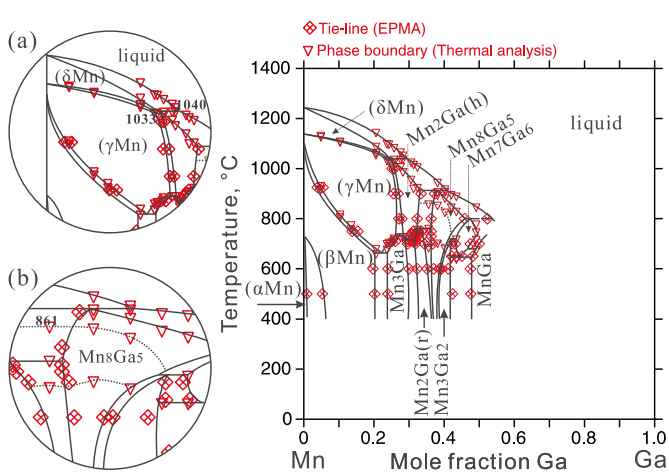

Fig. 5. The Mn–Ga phase diagram determined by Minakuchi et al. [19].

Other experimental investigations of the Mn–Ga phase diagram were reported by Masumoto et al. [23] and Tillard and Belin [24]. Masumoto et al. [23] established the partial Mn–Ga phase diagram between 19 and 31.2 at.% Ga below 800 °C. The phase transformation temperatures were determined based on thermal expansion and magnetization measurements. However, the tested samples were only homogenized at 850–900 °C for 30 min, and then cooled at the rate of 15–48 °C/h, without further annealing. And the samples for XRD analysis were only annealed at the interested temperature for 30 min. The Mn_3Ga phase was not observed, while the high-temperature phase Mn_2Ga(h) was reported to be stable down to the room temperature. Besides, this work failed to differentiate between Mn_2Ga(h) and Mn_3Ga, since these two phases have a similar crystal structure. Tillard and Belin [24] studied the phase equilibria in Mn–Ga alloys containing 75 to 100 at.% Ga. The stoichiometry of the phase with the highest Ga concentration was determined to be $MnGa_5$, instead of $MnGa_6$ as reported in the work of [16,17]. A polymorphic transformation from triclinic to the tetragonal structure was detected within the $MnGa_6$ phase at around 205 °C. An additional $MnGa_3$ phase was reported, but it was not studied in detail.

2.2. Existing discrepancies

One of the major differences among different versions of Mn–Ga phase diagrams is in the high-temperature range of the Mn-rich side, which is highlighted in Fig. 6. According to Meissner et al. [16] (Fig. 6 (a)), (δMn) reacts peritectically with liquid to form (γMn). However, Wachtel and Nier [17] (Fig. 6(b)) proposed that (δMn) decomposes metatectically into (γMn) and liquid. And it decomposes into (γMn) and Mn_2Ga(h), according to Minakuchi et al. [19] (Fig. 6(d)). The formation of Mn_2Ga(h) is due to a peritectic reaction between the (γMn) and liquid at around 1000 °C, according to Meissner et al. [16] (Fig. 6(a)) and Wachtel and Nier [17] (Fig. 6(b)), while Mn_2Ga(h) forms from a peritectic reaction between (δMn) and liquid at 1040 °C in the work of Minakuchi et al. [19] (Fig. 6(d)). As shown in Fig. 6(c), Lu et al. [18] proposed that (δMn) and (γMn) exist over a wide temperature and composition range, and no invariant reaction occurs from 950 to 1200 °C.

Two unknowns related to the Mn_8Ga_5 phase need to be confirmed, as indicated in Fig. 7. One is about the formation mechanism of the Mn_7Ga_6 phase. In Fig. 7(a), according to Meissner et al. [16], phase regions of Mn_8Ga_5 and Mn_7Ga_6 are incorporated since their stability range overlaps. However, as given in Fig. 7(b), Mn_7Ga_6 forms via a peritectic reaction between Mn_8Ga_5 and liquid based on the work by Wachtel and Nier [17]. As the temperature decreases, Mn_7Ga_6 decomposes into Mn_8Ga_5 and MnGa according to Wachtel and Nier [17] (Fig. 7(b)), while it decomposes into Mn_3Ga_2 and MnGa based on the measurement by Minakuchi et al. [19] (Fig. 7(c)). And the homogeneity range of Mn_7Ga_6 suggested by Wachtel and Nier [17] (Fig. 7(b)) is wider than that suggested by Minakuchi et al. [19] (Fig. 7(c)). The other unknown is the formation mechanism of the Mn_3Ga_2 phase. As shown in Fig. 7(a) and (b), this phase transforms directly from Mn_8Ga_5 at 650 °C based on the works of Meissner et al. [16] and Wachtel and Nier [17], while it forms via a reaction between Mn_8Ga_5 and Mn_7Ga_6 at 721 °C in the work of Minakuchi et al. [19], as revealed in Fig. 7(c). However, whether such a congruent transformation between two intermetallic compounds can happen needs further experimental validation.

Although Mn_3Ga is an important intermetallic compound due to its functional properties, its formation mechanism and stability range are yet unclear. The Mn_3Ga phase was not included in the phase diagram plotted by Meissner et al. [16]. In Fig. 8(a), Wachtel and Nier [17] suggested that Mn_3Ga forms peritectoidly from (βMn) and Mn_2Ga(r) at 510 °C, with relatively narrow temperature and composition ranges. However, this is different from the version by Lu et al. [18], which proposed that the temperature range of Mn_3Ga is below 820 °C and its formation is due to a congruent transformation from high-temperature (γMn) phase as shown in Fig. 8(b). The formation of Mn_3Ga

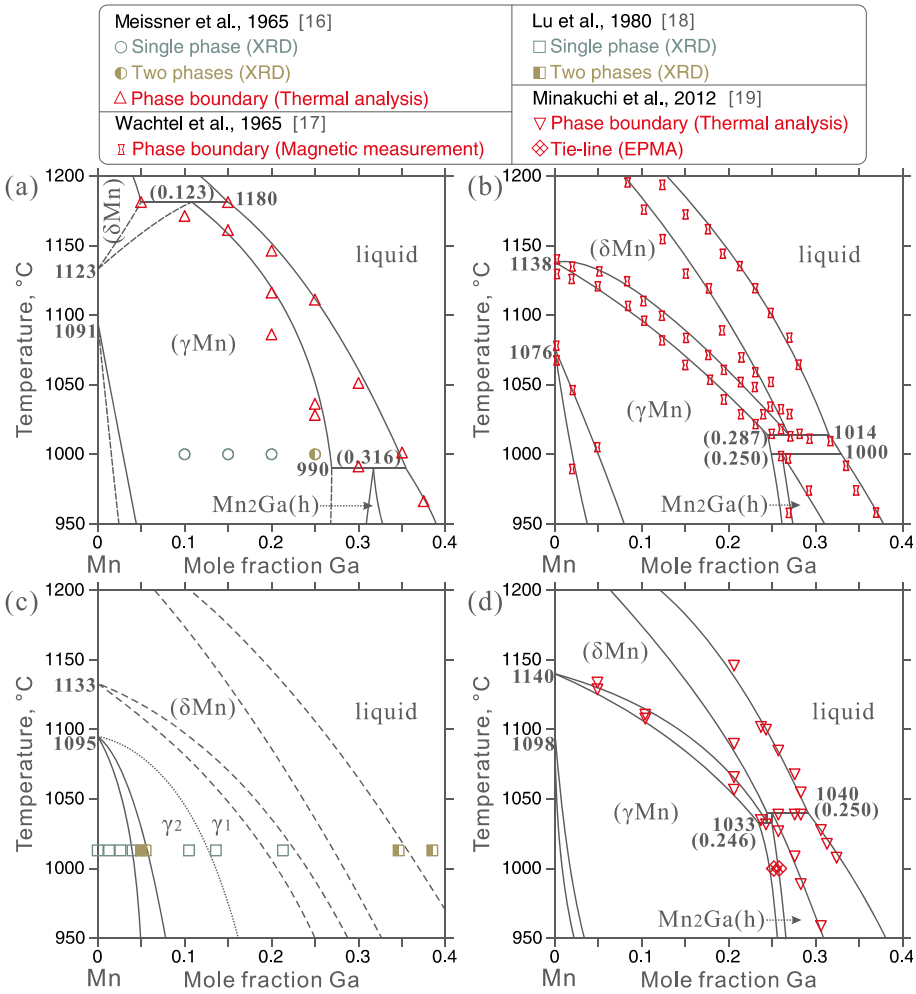

Fig. 6. High-temperature phase equilibria on the Mn-rich side according to the work of: (a) Meissner et al. [16]; (b) Wachtel and Nier [17]; (c) Lu et al. [18]; (d) Minakuchi et al. [19].

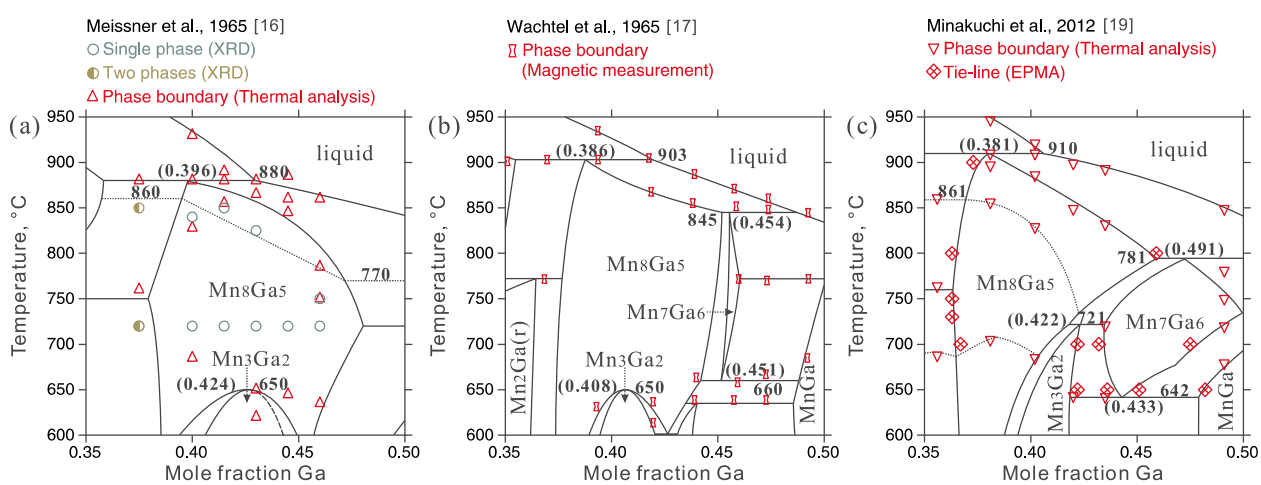

Fig. 7. Phase equilibria related to the Mn_8Ga_5 phase according to the work of: (a) Meissner et al. [16]; (b) Wachtel and Nier [17]; (c) Minakuchi et al. [19].

determined by Minakuchi et al. [19] (Fig. 8(c)) is distinctly different from the above two works. According to combined electron probe microanalysis (EPMA) and thermal analysis, the temperature range of Mn_3Ga is below 730 °C, and it forms from a peritectoid reaction between (γMn) and Mn_2Ga(h). In the work of Minakuchi et al. [19], Mn_3Ga can also react with Mn_2Ga(r) to form Mn_2Ga(h), as demonstrated in Fig. 8 (c).

The phase region of the MnGa phase is another unclear feature of the Mn–Ga phase diagram. Whether MnGa forms from a peritectic reaction between the liquid and Mn_8Ga_5 phases suggested by Meissner et al. [16] (Fig. 9(a)) or between liquid and Mn_7Ga_6 suggested by Wachtel and Nier [17] (Fig. 9(b)) needs to be studied further. The phase region of MnGa

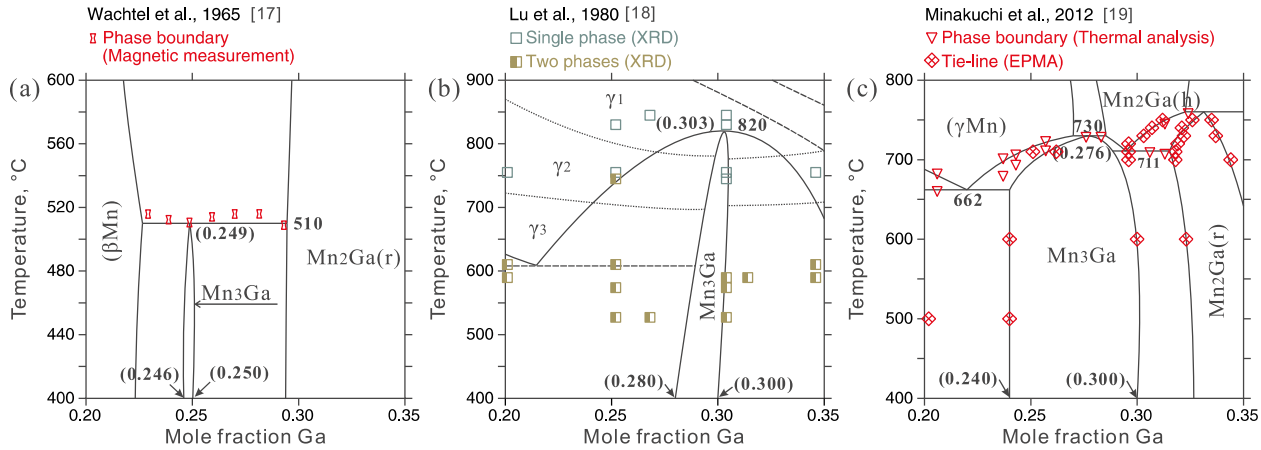

Fig. 8. The stability range of the Mn_3Ga phase according to the work of: (a) Wachtel and Nier [17]; (b) Lu et al. [18]; (c) Minakuchi et al. [19].

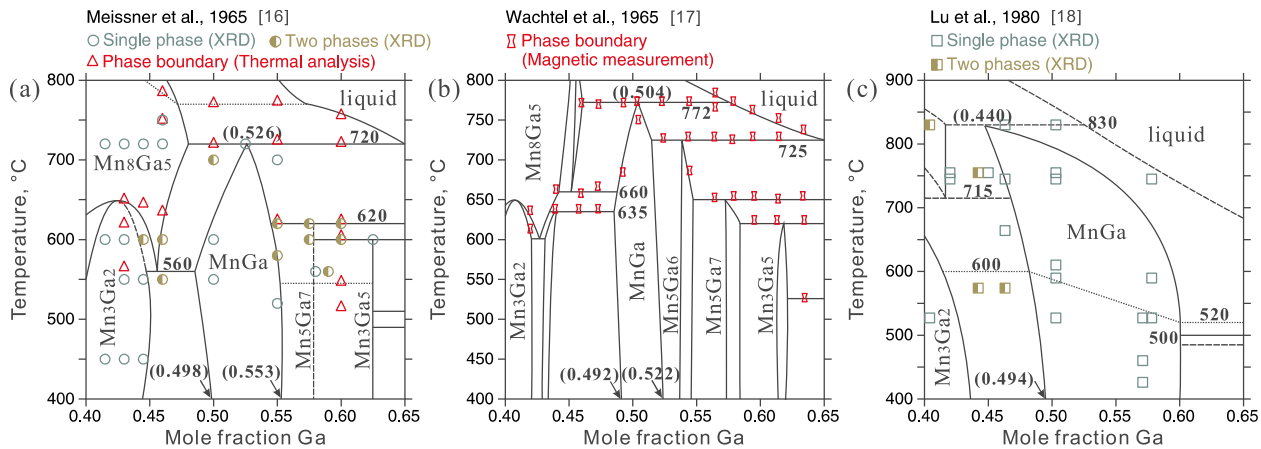

Fig. 9. The stability range of the MnGa phase according to the work of: (a) Meissner et al. [16]; (b) Wachtel and Nier [17]; (c) Lu et al. [18].

plotted by Lu et al. [18] in Fig. 9(c) is very wide, and it may cover other phases due to the difficulty in resolving complex XRD patterns. Besides, Lu et al. [18] determined that a polymorphic transformation within MnGa will occur between 520 and 600 °C. The work of Minakuchi et al. [19] did not cover complete phase equilibria information about MnGa.

2.3. Recommended Mn–Ga phase diagram

Okamoto [25] reviewed the literature related to experimental studies of the Mn–Ga phase diagram till the year 2012 and recommended a version of the Mn–Ga phase diagram incorporating the results of Minakuchi et al. [19] from 0 to 50 at.% Ga, the results of Meissner et al. [16] from 50 to 75 at.% Ga and the results of Tillard and Belin [24] from 75 to 100 at.% Ga. One problem of this recommended Mn–Ga phase diagram is that it includes the MnGa phase twice when combining works from different researchers. Both the MnGa phase in the work of Meissner et al. [16] and the λ phase in the work of Minakuchi et al. [19] correspond to the MnGa phase. The second problem is that it includes the $MnGa_3$ phase. However, the existence of this phase was only reported by Tillard and Belin [24], and thus needs to be further confirmed. Finally, it accepts the work of Meissner et al. [16] but fails to include the Mn_5Ga_6 phase. In fact, the existence of this phase has been confirmed by several researchers [17,26,27].

After a critical evaluation of the experimental information available in the literature, an updated version of the Mn–Ga phase diagram is recommended in this study (Fig. 10). The Mn-rich side (0 to 50 at.% Ga) is based on the results of Minakuchi et al. [19], since this work used the accurate experimental technique, namely EPMA, to measure the phase composition. Besides, compared with others' work [16–18], Minakuchi et al. [19] used a longer duration, varying from 3 h at 1000 °C to 30 days at 500 °C, to anneal the samples, which is more likely to reach the equilibrium state. Finally, the formation of Mn_3Ga_2 via a peritectoid reaction between Mn_8Ga_5 and Mn_7Ga_6 is more reasonable than via a direct phase transformation from Mn_8Ga_5, which was suggested by Refs. [16,17]. The Ga-rich side (50 to 100 at.% Ga) is based on the results of Wachtel and Nier [17], because this work agrees well with that of Minakuchi et al. [19] on the Mn-rich side and includes all the reported Ga-rich phases. Meanwhile, the purity of raw materials used by Wachtel and Nier [17] is the highest among the four works discussed above. However, as the work of Wachtel and Nier [17] did not provide any experimental information related to the determination of the homogeneity ranges of Ga-rich intermetallic compounds, these phases are all simplified as line compounds in the recommended phase diagram in this work. Phase regions with dense clusters of experimental data points are magnified in Fig. 10(b), (c), and (d).

Based on the Mn–Ga phase diagram recommended in this work, there are seventeen invariant reactions, as listed in Table 2. The phase equilibria on the Ga-rich side is relatively simple, with all phases forming from a peritectic reaction. On the contrary, the phase equilibria on the Mn-rich side is complex and has not been confirmed experimentally, which is probably due to the high vapor pressure of Mn-rich alloys. These two complications will cause difficulty in phase diagram determination on the Mn-rich side. Further experiments need to be performed to address the following problems: (1) Which type of phase reaction occurs among the liquid, (γMn), and (δMn) phases? (2) Does the Mn_7Ga_6 phase exist? If so, how does it react with the Mn_8Ga_5 phase? (3) Does the

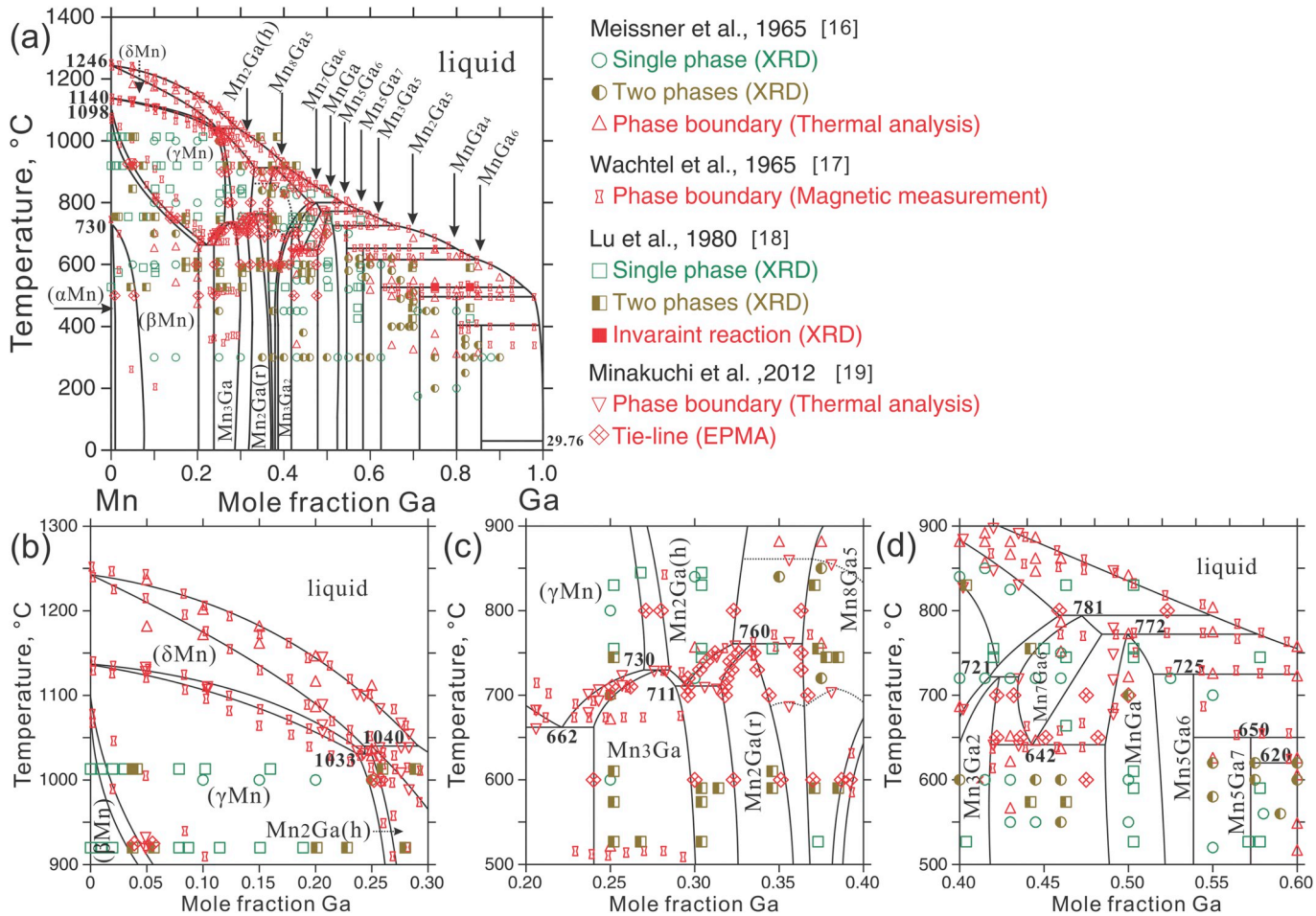

Fig. 10. (a) A new version of the Mn–Ga phase diagram recommended in this work. Magnified parts in (b), (c), and (d) are phase regions with dense clusters of experimental data points.

Table 2
Invariant reactions in the Mn–Ga system.

Reaction	T [°C]	Composition [at.% Ga]		
L + (δMn) ⇌ Mn_2Ga(h)	1040	29.3	24.6	25.0
(δMn) ⇌ Mn_2Ga(h) + (γMn)	1033	24.6	25.0	23.9
L + Mn_2Ga(h) ⇌ Mn_8Ga_5	910	40.2	33.1	38.0
L + Mn_8Ga_5 ⇌ Mn_7Ga_6	781	53.8	46.0	46.9
Mn_8Ga_5 + Mn_2Ga(h) ⇌ Mn_2Ga(r)	760	36.3	32.2	33.4
Mn_2Ga(h) + (γMn) ⇌ Mn_3Ga	730	28.4	27.1	27.9
Mn_8Ga_5 + Mn_7Ga_6 ⇌ Mn_3Ga_2	721	41.6	43.5	42.2
Mn_2Ga(h) ⇌ Mn_2Ga(r) + Mn_3Ga	711	29.4	31.4	28.9
(γMn) ⇌ (βMn) + Mn_3Ga	662	22.2	20.1	24.1
Mn_7Ga_6 ⇌ MnGa + Mn_3Ga_2	642	44.3	47.7	41.7
L + Mn_7Ga_6 ⇌ MnGa	772	57.9	46.0	50.3
L + MnGa ⇌ Mn_5Ga_6	725	64.7	51.5	53.8
L + Mn_5Ga_6 ⇌ Mn_5Ga_7	650	78.9	54.7	57.4
L + Mn_5Ga_7 ⇌ Mn_3Ga_5	620	82.7	58.3	61.7
L + Mn_3Ga_5 ⇌ Mn_2Ga_5	522	95.4	62.1	70.0
L + Mn_2Ga_5 ⇌ $MnGa_4$	498	97.9	70.3	79.6
L + $MnGa_4$ ⇌ $MnGa_6$	400	99.1	80.0	85.2

Mn_3Ga_2 phase can really form by a congruent transformation from the Mn_8Ga_5 phase? (4) The stability range, homogeneity range, and formation mechanism of the Mn_3Ga phase. (5) The stability range, homogeneity range, and formation mechanism of the MnGa phase.

3. Crystallography

In contrast to the limited reports related to the phase equilibria of the Mn–Ga system, there are extensive studies about the crystal structure of the Mn–Ga phases. The relevant studies are summarized in Table 3.

3.1. Structure of intermetallic compounds

Table 4 summarizes the crystallographic information of the Mn–Ga intermetallic compounds. As revealed, the Mn_3Ga and MnGa phases can adopt different structures as the alloy composition or the processing condition changes. Whether the Mn_8Ga_5 phase is primitive or body-centered cubic is still unclear. The following text will discuss in detail the crystal structure of intermetallic compounds in the Mn–Ga system.

Mn_3Ga has been reported to have three structures, namely, hexagonal, tetragonal, and cubic (Fig. 11). Hexagonal Mn_3Ga with $D0_{19}$ ordering ($P6_3/mmc$) can be obtained in the water-quenched alloys containing 26 to 30 at.% Ga between 600 and 800 °C [28–32]. Niida et al. [31,32] detected an orthorhombic distortion within the hexagonal Mn_3Ga phase at −157 to 59 °C based on the temperature dependence of the lattice constant and magnetization. A structural transition at −88 °C was also observed in melt-spun ribbons containing 30 at.% Ga [33]. According to the thermal analysis, an order-disorder transition occurs in the hexagonal Mn_3Ga phase at 652–727 °C in arc-melted alloys with 25–33.3 at.% Ga [34]. After annealing alloys containing 23.5–31.2 at.% Ga at 350–450 °C, tetragonal Mn_3Ga with $D0_{22}$ ordering ($I4/mmm$) will precipitate from the high-temperature (γMn) phase [35,36]. Recently, DFT (density functional theory) calculations [37,38] predicted the

Table 3
Experimental studies and atomistic modeling relevant to the crystal structure and magnetic properties of the Mn-Ga intermetallic compounds.

Phases	Properties Studied	Methods	Ref.
Mn_3Ga, MnGa, $MnGa_3$	Structure		[28]
Mn_2Ga_5	Structure		[73]
Mn_8Ga_5	Structure, magnetic	XRD, magnetic measurement	[42]
Mn_3Ga	Structure, magnetic	XRD, magnetic measurement	[29]
Mn_3Ga_2	Structure, magnetic	XRD, magnetic measurement	[64]
Mn_2Ga(r), Mn_3Ga_2	Structure		[74]
Mn_2Ga(r)	Structure, magnetic	XRD, magnetic measurement	[65]
Mn_3Ga_2	Structure, magnetic	XRD, magnetic measurement	[75]
All	Structure	XRD	[16]
All	Magnetic	Magnetic measurement	[17]
Mn_3Ga	Structure, magnetic	Neutron diffraction	[30]
Mn_2Ga_5	Structure	XRD	[67]
Mn_2Ga_5	Structure, magnetic	Neutron diffraction, magnetic measurement	[68]
Mn_3Ga	Structure, magnetic	XRD, thermal expansion, magnetic measurements	[35]
Mn_3Ga_2	Structure	XRD	[76]
Mn_3Ga_2, $MnGa_4$	Structure, magnetic	XRD, magnetic measurement	[18]
Mn2Ga(h), Mn2Ga(r), MnGa	Structure, magnetic, magneto-optical	XRD, magnetic and Kerr effect measurements	[77]
Mn_3Ga	Structure, magnetic	XRD, magnetic measurement	[31]
Mn_3Ga	Structure, magnetic	XRD, magnetic measurement	[32]
Mn_2Ga5	Structure	TEM, thin film	[69]
Mn_3Ga	Structure, magnetic	XRD, magnetic measurement	[36]
MnGa, Mn_5Ga_6, Mn_5Ga_7, Mn_3Ga_5	Structure, magnetic	TEM	[26]
Mn_5Ga_6	Structure	HREM	[27]
MnGa	Magnetic	DFT (LMTO)	[46]
MnGa	Structure	HREM	[53]
MnGa	Magnetic	DFT (LAPW)	[47]
Mn_3Ga_5	Structure	XRD, single crystal	[55]
Mn_5Ga_7	Structure	HREM	[54]
MnGa	Structure	XRD, single crystal	[57]
$MnGa_4$	Structure, magnetic	XRD, magnetic measurement, DFT	[52]
Phases	Properties Studied	Methods (LAPW)	Ref.
Mn_3Ga_5	Structure		[56]
MnGa	Structure, magnetic	XRD, single crystal, DFT (LMTO)	[45]
Mn_3Ga	Magnetic	DFT (LSDA)	[37]
Mn_3Ga	Structure, magnetic	DFT (LAPW)	[38]
Mn_3Ga	Structure, magnetic	XRD, magnetic measurement, DFT (LAPW)	[13]
Mn_2Ga_5	Structure, magnetic	XRD, single crystal, magnetic measurement, DFT (FPLO)	[70]
Mn_3Ga	Structure, magnetic	XRD, EXAFS, magnetic measurement, DFT (SPRKKR)	[34]
Mn_3Ga	Structure, magnetic	XRD, magnetic measurement, melt-spun ribbon	[44]
MnGa	Structure, magnetic	XRD, SEM, magnetic measurement, microparticle	[50]
Mn_3Ga	Structure, magnetic	XRD, magnetic measurement, melt-spun ribbon	[39]
Mn3Ga, Mn2Ga(r)	Structure, magnetic	XRD, TEM, magnetic measurement, melt-spun ribbon	[51]
Mn_3Ga	Structure, magnetic	XRD, neutron diffraction, XAS, magnetic measurement, thin film, DFT (LAPW)	[78]
Mn_3Ga	Structure	DFT (LAPW, VASP)	[41]
Mn_8Ga_5, Mn_3Ga	Magnetic	XRD, magnetic measurement, melt-spun ribbon	[33]
Mn_3Ga	Structure, magnetic	XRD, SEM, magnetic measurement, DFT (VASP), melt-spun ribbon	[40]
Mn_3Ga_2	Magnetic	XRD, magnetic measurement	[66]
Mn_3Ga	Structure, magnetic	XRD, magnetic measurement	[62]
Mn_3Ga	Structure, magnetic	XRD, TEM, magnetic measurement	[79]
Mn3Ga, Mn2Ga(r)	Structure, magnetic	XRD, TEM, magnetic measurement, melt-spun ribbon	[49]
MnGa	Structure, magnetic	XRD, magnetic measurement	[12]
Mn_8Ga_5	Structure, magnetic	XRD, SEM, magnetic measurement, DFT (VASP)	[43]
Mn_3Ga	Structure, magnetic	DFT (pseudopotential method)	[63]

Abbreviations: TEM, transmission electron microscopy; HREM, high-resolution electron microscopy; DFT, density functional theory; LMTO, linearized muffin-tin orbital method; LAPW, linearized augmented plane-wave method; LSDA, local spin-density functional approximation; FPLO, full-potential local orbital method; XAS, X-ray absorption spectroscopy; SPRKKR, spin polarized fully relativistic Korringa-Kohn-Rostoker method; SEM, scanning electron microscopy; VASP, Vienna *ab initio* simulation package.

existence of a cubic Mn_3Ga. This $D0_3$-type cubic phase has the same structure as Heusler compounds ($Fm\bar{3}m$) and was observed in melt-spun ribbons with 25 at.% Ga [39]. Kharel et al. [40] systematically investigated the structural, magnetic and electronic properties of the cubic Mn_3Ga phase using experiments and theoretical calculations. The XRD patterns revealed a disordered structure, isostructural with Cu_3Au ($Pm\bar{3}m$), for cubic Mn_3Ga. They also proposed that this cubic phase transforms into tetragonal $D0_{22}$-Mn_3Ga at 327 °C then into hexagonal $D0_{19}$-Mn_3Ga at 527 °C. Accompanied by the structural transformation, the magnetic state of the Mn_3Ga ribbon changes from paramagnetic to ferrimagnetic then back to paramagnetic. The substitutional disordering within melt-spun Mn_3Ga ribbons was then confirmed using DFT calculations by Kharel et al. [40], which demonstrated that the paramagnetism of cubic Mn_3Ga stems from the opposite sign of the magnetic moments of Mn atoms on different sites. Using DFT, Zhang et al. [41] optimized the lattice parameters for the three structures of Mn_3Ga and compared their stability based on the variation of total energy with volume. In contrast to the results of Kharel et al. [40], this study proposed a successive structural transition from hexagonal $D0_{19}$-Mn_3Ga to cubic $D0_3$-Mn_3Ga then to tetragonal $D0_{22}$-Mn_3Ga as the annealing temperature decreases.

The crystal structure of the Mn_8Ga_5 phase was firstly determined by

Table 4
Crystallographic data of the Mn–Ga intermetallic compounds.

Phase/Temperature Range [°C]	Pearson Symbol/Space Group/Prototype	Lattice Parameters [Å]	Composition [at.% Ga]	References
(αMn) <730	*cI*58 $I\bar{4}3m$ α-Mn	$a = 8.912$		[16]
(βMn) <1098	*cP*20 $P4_132$ β-Mn	$a = 6.375$	15	[16]
(γMn) 662–1140	*cF*4 $Fm\bar{3}m$ Cu	$a = 3.769$	25	[16]
(δMn) 1033–1244	*cI*2 $Im\bar{3}m$ W	$a = 3.080$		[16]
Mn_3Ga <730	*hP*8 $P6_3/mmc$ Ni_3Sn	$a = 5.363$, $c = 4.327$ $\gamma = 120°$	28.75 (Quenched from 800 °C)	[30]
	*tI*8 $I4/mmm$ Al_3Ti	$a = 3.901$, $c = 7.120$	28.75 (Annealed at 1023 °C)	[30]
	*cF*16 $Fm\bar{3}m$ $AlFe_3$	$a = 5.8232$	(Calculated)	[38]
Mn_2Ga(h) 711–1040	*hP*2 $P6_3/mmc$ Mg	$a = 2.678$, $c = 4.338$ $\gamma = 120°$	30	[16]
Mn_2Ga(r) <760	*tP*4 $P4/mmm$ AuCu	$a = 3.898$, $c = 3.586$		[16]
Mn_8Ga_5 <910	*cI*52 $I\bar{4}3m$ Cu_5Zn_8	$a = 8.992$	38	[42]
	*cP*52 $P\bar{4}3m$ Al_4Cu_9	$a = 9.023$	40.2	[19]
Mn_3Ga_2 <721	*tP*2 $P4/mmm$ AuCu	$a = 2.755$, $c = 3.666$	40.2	[19]
Mn_7Ga_6 642–781	*hR*78 $R\bar{3}mh$	$a = 12.602$, $c = 8.056$ $\gamma = 120°$	43.5	[19]
MnGa <772	*hR*26 $R3m$ Al_8Cr_5	$a = 12.587$, $c = 8.035$ $\gamma = 120°$		[28]
	*hR*78 $R\bar{3}m$	$a = 12.605$, $c = 8.0424$ $\gamma = 120°$	52	[45]
	*mS*276 $C12/c1$	$a = 20.157$, $b = 14.718$, $c = 14.889$ $\beta = 121.349°$	49.1	[19]
	*oC** $Bmmm$	$a = 20.4$, $b = 12.5$, $c = 14.8$	54	[26]
	*m***	$a = 25.9$, $b = 12.5$, $c = 11.5$ $\beta = 110°$	52	[26]
	*tP*4 $P4/mmm$ AuCu	$a = 3.8921$, $c = 3.6920$	45	[12]
Mn_5Ga_6 <725	*oP** $Pnma$ Al_3Mn	$a = 12.6$, $b = 12.5$, $c = 14.8$	55	[26]
	*oC** $Bmmb$ $Al_{60}Mn_{11}Ni_4$	$a = 7.7$, $b = 12.5$, $c = 23.6$	57	[26]
Mn_5Ga_7 <650	*oC** $Bmm2$	$a = 45.7$, $b = 12.5$, $c = 14.4$	58	[26]
Mn_3Ga_5 <620	*tP** $P4_2/n2_1c$	$a = 12.5$ $c = 25.0$	62	[26]
Mn_2Ga_5 <522	*tP*14 $P4/mbm$ Hg_5Mn_2	$a = 8.803$, $c = 2.694$	71	[73]
$MnGa_4$ <498	*cI*10 $Im\bar{3}m$ Hg_4Pt	$a = 5.591$	80	[16]
$MnGa_6$ <400		$a = 8.949$, $b = 8.814$, $c = 9.944$	86	[16]

(*continued on next page*)

Table 4 (*continued*)

Phase/Temperature Range [°C]	Pearson Symbol/Space Group/Prototype	Lattice Parameters [Å]	Composition [at.% Ga]	References
	*oC*28 *Cmcm* Al_6Mn			
Ga <30	*oC*8 *Cmca* Ga	$a = 4.5199$, $b = 7.6603$; $c = 4.5259$		[80]

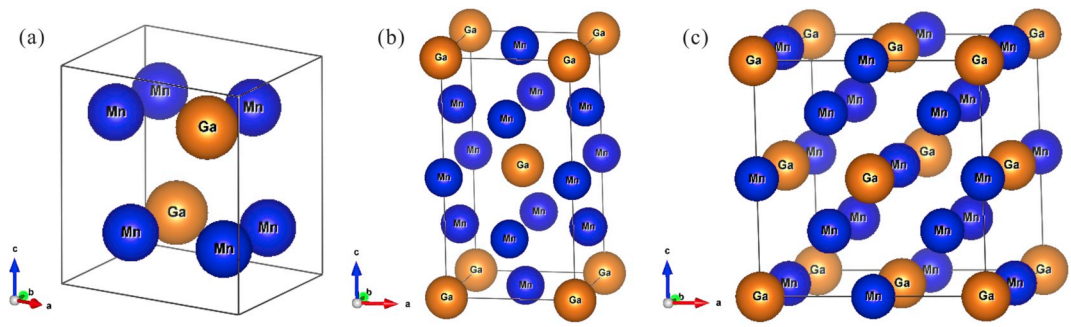

Fig. 11. Three possible structures for the Mn_3Ga phase: (a) hexagonal lattice with $D0_{19}$ ordering; (b) tetragonal lattice with $D0_{22}$ ordering; (c) cubic lattice with $D0_3$ ordering. Blue atoms are Mn. Orange atoms are Ga. (For interpretation of the references to colour in this figure legend, the reader is referred to the Web version of this article.)

Tsuboya and Sugihara [42] as γ-brass type (body-centered cubic). However, Meissner et al. [16] suggested that the structure of Mn_8Ga_5 is not a perfect γ-brass type due to the presence of reflection patterns from a hexagonal lattice. They also proposed that when the temperature or the Ga content increases, the structure of Mn_8Ga_5 transforms into the Al_8Cr_5 type (rhombohedral). A two-stage order-disorder transition within the Mn_8Ga_5 phase was reported by Minakuchi et al. [19]. However, only the low-temperature Mn_8Ga_5 can be synthesized as the single-phase and it has a similar structure to Al_4Cu_9. This result was supported by Tozman et al. [43] using both experiments and DFT calculations. In their work, several alloys were prepared under different annealing and cooling conditions to obtain the Mn_8Ga_5 phase stable at different temperatures. The XRD patterns revealed that these phases have the same structural symmetry but differ in the degree of atomic ordering. Further studies are still needed to confirm that the processing condition used in their study is effective to maintain the high-temperature and moderate-temperature Mn_8Ga_5 phases in the single-phase state. The structural model formulated by Tozman et al. [43] based on the DFT calculations is similar to a layered tetragonal unit cell with $L1_0$ ordering, which explains why Mn_8Ga_5 usually co-exists with other $L1_0$-type phases in the Mn–Ga alloys [12,33,44].

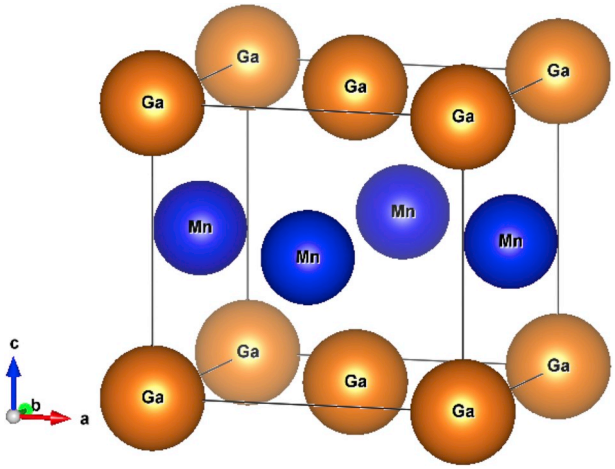

Fig. 12. The MnGa phase with $L1_0$ ordering. Blue atoms are Mn. Orange atoms are Ga. (For interpretation of the references to colour in this figure legend, the reader is referred to the Web version of this article.)

Reports [19,26,28,45–47] about the crystal structure of the MnGa phase disagree with each other, which may be due to the polymorphism of MnGa. Schubert et al. [28] determined the structure of MnGa to be the same as Al_8Cr_5 ($R3m$), which can be indexed with either the hexagonal or rhombohedral axis. A different space group, $R\bar{3}m$, was suggested by Gourdon and Miller [45] based on the single-crystal XRD analysis. Other structural parameters, including the atomic coordinates, displacements, and interatomic distance were refined using the $R\bar{3}m$ symmetry. Minakuchi et al. [19] determined the crystal structure of MnGa as monoclinic with a large unit cell. This phase was reported to relate to the decagonal quasicrystal and adopt an orthorhombic or a monoclinic structure with the same lattice constant b by Wu and Kuo [26]. Using DFT calculations, the MnGa phase was predicted to adopt the AuCu type structure with $L1_0$ ordering [46,47]. Due to its extraordinary magnetic performance, several researchers have successfully synthesized the $L1_0$-type MnGa phase in bulk alloys [12], thin films [6,10,48], melt-spun ribbons [39,49], and mechanically milled powders [12,50]. It needs to be mentioned here that both Mn_2Ga(r) and Mn_3Ga_2 phases have the $L1_0$-type ordered structure similar to AuCu, and their phase regions are close to each other. Thus, the $L1_0$-type MnGa phase described in this and the following sections is not the same as that indicated in the Mn–Ga phase diagram. The $L1_0$-type MnGa phase here refers to the Mn–Ga intermetallic compounds with the $L1_0$-type crystal structure, and thus includes the Mn_2Ga(r), Mn_3Ga_2 and MnGa phases as denoted in Fig. 10.

The unit cell of the MnGa phase with $L1_0$ ordering is illustrated in Fig. 12. It has a tetragonal structure with similar lattice constants a and c. Indeed, the structure of tetragonal $L1_0$-type MnGa is closely related to that of tetragonal $D0_{22}$-Mn_3Ga. The lattice parameters a for both phases are almost the same, while the lattice parameter c for $D0_{22}$-Mn_3Ga is around two times the value of c for $L1_0$-type MnGa [36]. Therefore, for different applications, it is convenient to synthesize either $L1_0$-type MnGa or $D0_{22}$-Mn_3Ga by tuning the alloy composition. For example, Niida et al. [36] obtained the $L1_0$-type phase in annealed alloys with 36 to 37 at.% Ga, and the $D0_{22}$-type phase in annealed alloys with 26 to 34

at.% Ga. Huh et al. [51] determined that the melt-spun Mn–Ga ribbons exhibit the $L1_0$ structure when the Ga content is 38 to 45 at.%, and the $D0_{22}$ structure when the Ga content is 34 at.%.

The crystal structure of $MnGa_4$ was firstly reported by Schubert et al. [28], with the ideal composition of $MnGa_3$. Later, Meissner et al. [16] suggested the stoichiometric composition of this phase to be $MnGa_4$, and confirmed the structure to be Hg_4Pt type with the space group $Im\bar{3}m$. As a representative of Hume-Rothery compounds, structural parameters of $MnGa_4$ were refined using the XRD analysis and DFT calculations by Häussermann et al. [52]. Tillard and Belin [24] studied the structural properties of $MnGa_4$ using single-crystal XRD data, and constructed its structure by packing the cubic subunit of Ga atoms with a Mn atom in the center.

The stoichiometric composition of the phase with the highest content of Ga was determined to be $MnGa_6$ by Meissner et al. and Wachtel and Nier [16,17], but its structure was not resolved in these two studies. A polymorphic transformation at 340–385 °C within this phase was reported by Wachtel and Nier [17]. Lu et al. [18] assumed that the stoichiometry of this phase should be either $MnGa_5$ or Mn_2Ga_9. This assumption was confirmed by Tillard and Belin [24], which determined that the stoichiometric composition of the phase with the highest content of Ga is closer to $MnGa_5$, instead of $MnGa_6$. Besides, this phase has two structural modifications: tetragonal $MnGa_{4.96}$ and triclinic $MnGa_{4.83}$. The structures of these two modifications can be constructed based on subunits with a square antiprismatic shape.

3.2. Decagonal quasicrystal (DQC) approximants

Due to the similarity with the Al–Mn system in which the first quasicrystals were reported, the Mn–Ga system is also featured by the existence of DQC in rapidly solidified alloys. Wu and Kuo [26] successfully synthesized DQC in the melt-spun ribbons containing 52 to 58 at.% Ga, and proposed that in contrast to the Al–Mn DQC, the Mn–Ga DQC is metastable and can coexist with other intermetallic compounds in water-quenched alloys.

The crystal structures of many Ga-rich intermetallic compounds, including MnGa, Mn_5Ga_6, Mn_5Ga_7, and Mn_3Ga_5, are related to that of Mn–Ga DQC. These intermetallic compounds consist of the same subunits as that of Mn–Ga DQC, but they exhibit both the translational and rotational symmetries. Meanwhile, these decagonal subunits are packed

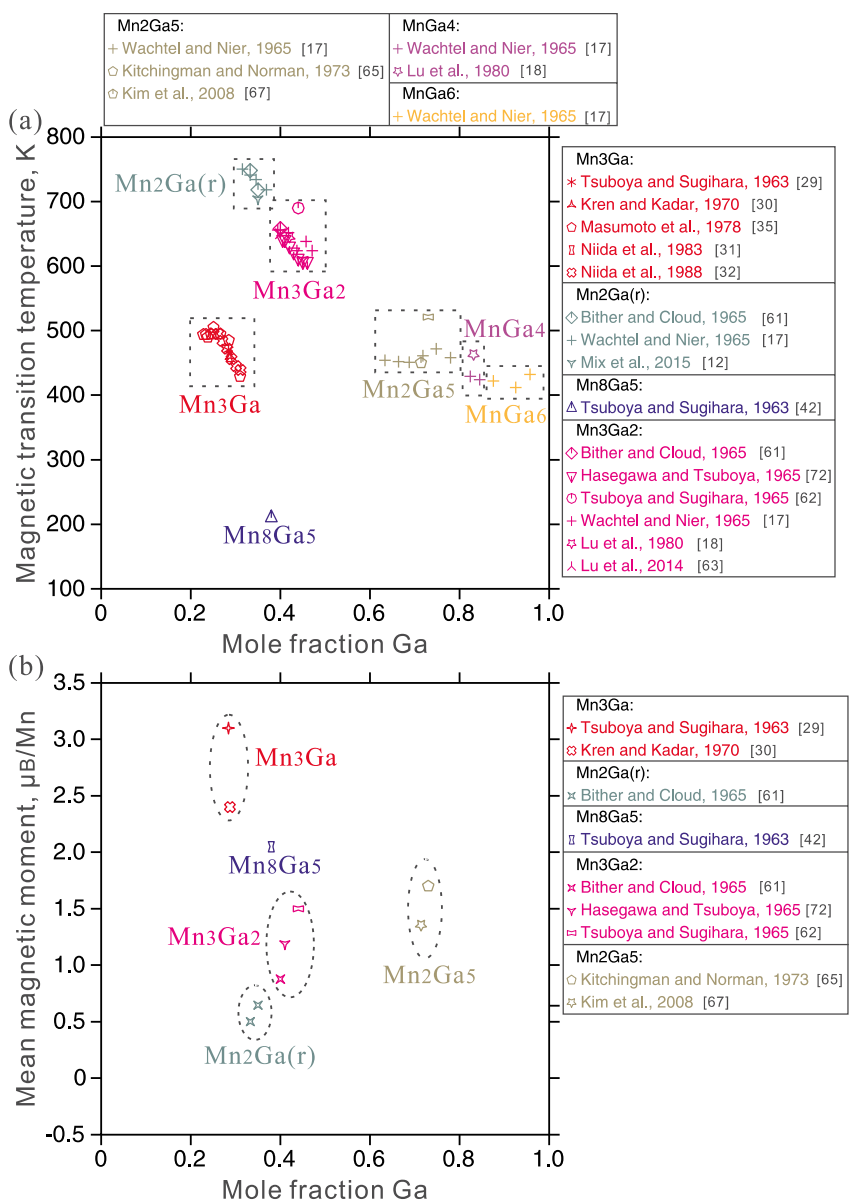

Fig. 13. Magnetic properties of the Mn–Ga intermetallic compounds: (a) magnetic transition temperature; (b) mean magnetic moment.

in a periodic way within these intermetallic compounds, while they are packed aperiodically in the Mn–Ga DQC. Therefore, these Mn–Ga intermetallic compounds are called DQC approximants. Wu and Kuo [26] demonstrated that all these Mn–Ga DQC approximants have a large unit cell, with the lattice parameter *b* equal to the tenfold axis periodicity of the Mn–Ga DQC.

The Mn_5Ga_6 DQC approximant has two structural variants: primitive and B-centered orthorhombic. Built on the basis of the same subunits these two structural variants often coexist and produce tenfold twins [26]. Using the high-resolution electron microscopy, Wu et al. [53] constructed the structural model for the Mn_5Ga_6 DQC approximant by the hexagonal subunits. If the subunits orient along the same direction, a B-centered lattice forms; If the subunits orient along with two different directions alternately, a primitive lattice forms. Based on the proposed structural models, Wu et al. [53] simulated the diffraction patterns and electron images, which agree well with the experimental observations.

The structural model of the Mn_5Ga_7 DQC approximant was resolved by Wu and Kuo [54]. They found that the one-face-centered orthorhombic Mn_5Ga_7 consists of differently oriented hexagonal subunits, which are separated by subunits with a crown shape.

Boström and Hovmöller [55] refined the structural parameters for the tetragonal Mn_3Ga_5 DQC approximant using the single-crystal XRD data. The unit cell of Mn_3Ga_5 was constructed based on the alternate arrangement of a cluster existing in γ-brass and a rod-shaped subunit existing in $Cr_{23}C_6$. Uchida and Matsui [56] proposed a new perspective to understand the structure of DQC approximants, and used this method to analyze the structure of Mn_3Ga_5. In their work, the large unit cell of Mn_3Ga_5 DQC approximant was constructed by stacking close-packed layers over which the vacancy sites are distributed in an ordered manner, rather than by packing the subunits, as suggested by Boström and Hovmöller [55].

According to Wu and Kuo [26], the MnGa DQC approximant can adopt the orthorhombic and monoclinic structures. These two invariants exhibit certain orientation relationship, so the structural transition can easily occur by introducing the stacking faults. The structural parameters of the monoclinic MnGa DQC approximant were refined based on the single-crystal XRD patterns by Boström and Hovmöller [57], who also constructed the unit cell of this DQC approximant by packing the wheel-shaped pentagonal subunits in planes perpendicular to the pseudo five-fold axis.

4. Magnetic properties

The intrinsic magnetic properties of a phase can have a significant influence on its total Gibbs free energy, which determines its phase equilibria with other phases. For example, an additional miscibility gap can occur in some phase diagrams such as Fe-Ni [58] and Fe–Cr [59,60] owing to magnetic ordering energy contribution [61]. The Mn–Ga system is featured by the richness of magnetic phases. Therefore, the magnetic properties of these phases are critically reviewed, in order to accurately calculate the magnetic contributions to the Gibbs free energy and the magnetic phase diagram of the Mn–Ga system.

A majority of Mn–Ga intermetallic compounds, namely, Mn_3Ga, Mn_2Ga(h), Mn_2Ga(r), Mn_8Ga_5, Mn_3Ga_2, MnGa, Mn_3Ga_5, Mn_2Ga_5, $MnGa_4$, and $MnGa_6$, have been reported to be magnetic. Meissner et al. [16] suggested that Mn_2Ga(h) is ferromagnetic, but since then, no study about the magnetic properties of Mn_2Ga(h) was conducted. Other magnetic phases that are stable till the room temperature were investigated extensively for applications in magnetic thin films, permanent magnets, and spintronic devices. After a comprehensive review of reported magnetic properties, the magnetic transition temperature and the mean magnetic moment for several Mn–Ga intermetallic compounds are summarized in Fig. 13. As can be shown, the unit of the magnetic transition temperature in Fig. 13 is Kelvin, so this unit will be used to describe the Curie and Néel temperatures for the Mn–Ga intermetallic compounds in the following sections. These data are critical to the CALPHAD-type (Calculation of Phase Diagrams) assessment of the Mn–Ga system [61]. However, one needs to keep in mind that the revised Inden-Hillert-Jarl model proposed by Xiong et al. [61] for the CALPHAD approach considers the effective magnetic moment but not mean magnetic moment, which has been proved as the wrong physical quantity for magnetic entropy estimation. Therefore, some DFT calculations are required to obtain local magnetic moment for estimation of the effective magnetic moment during the CALPHAD modeling.

As mentioned earlier, Mn_3Ga can exhibit three structures, depending on the composition range and the processing condition. Their magnetic properties differ significantly: $D0_{19}$-Mn_3Ga is antiferromagnetic with the Néel temperature of 460 K and the magnetic moment of 2.4 μ_B/Mn [30]; $D0_{22}$-Mn_3Ga is ferrimagnetic and it is characterized by the high Curie temperature and low magnetization; $D0_3$-Mn_3Ga is ferrimagnetic with a Curie temperature of 314 K [37], and a magnetic moment of −0.003 μ_B/Mn [38,41].

Krén and Kádár [30] resolved the spin configurations for $D0_{19}$-and $D0_{22}$-Mn_3Ga using the neutron diffraction. $D0_{19}$-Mn_3Ga has a triangular antiferromagnetic arrangement of Mn magnetic moments in the basal plane of the hexagonal lattice. In contrast, $D0_{22}$-Mn_3Ga aligns all magnetic moments with the opposite sign along the *c* axis of the tetragonal lattice. Besides, Krén and Kádár [30] suggested that the weak ferromagnetism of $D0_{19}$-Mn_3Ga observed below the Néel temperature by Tsuboya and Sugihara [29] and Niida et al. [31] stems from the distortion of the triangular magnetic structure.

Niida et al. [31] detected an orthorhombic distortion within the hexagonal $D0_{19}$-Mn_3Ga, and such a structural transition leads to a steep increase in the spontaneous magnetization. The same researchers [32] used the XRD analysis and magnetization measurement to determine the Néel and structural distortion temperatures for the $D0_{19}$-Mn_3Ga phase in the composition range of 24 to 32 at.% Ga as shown in Fig. 13 (a).

Since the Curie temperature for $D0_{22}$-Mn_3Ga is higher than the structural transition temperature (770 K) from $D0_{22}$-to $D0_{19}$-Mn_3Ga, it is difficult to measure it via experiments. Kübler [37] estimated the Curie temperature of $D0_{22}$-Mn_3Ga to be 762 K, using the DFT method. Winterlik et al. [34] studied the effect of the deficiency in Mn atoms on the magnetic properties of alloys with the $D0_{22}$-type structure. As the content of Mn decreases, the coercive force and maximum energy product will decrease, while the magnetization will increase. That confirmed the magnetic structure predicted through the DFT calculations. There are two crystallographically inequivalent sites for the Mn atoms, and their magnetic moments align in the opposite direction. As the reduction in the Mn content, more Mn atoms are removed from one site than the other, leading to the increased magnetization. Wei et al. [62] investigated the composition dependence of magnetization in $Mn_{3-x}Ga$ ($x = 0$ to 1.15) series of alloys. They proposed that the increase in the magnetization with the decrease in the Mn content is due to the preferential substitution of Ga for Mn at specific crystallographic sites, rather than the introduction of vacancies. Meanwhile, their work achieved the coercivity at the room temperature as high as 18.2 kOe by pressing and annealing the cast ingot with 25 at.% Ga.

Ferrimagnetic $D0_3$-Mn_3Ga has a structure ($Fm\bar{3}m$) similar to that of Heusler compounds, and hence, the magnetic moments are highly localized. Local magnetic moments of Mn atoms at Wyckoff positions 4*b* (1/2, 1/2, 1/2) and 8*c* (1/4, 1/4, 1/4) are 3.03 μ_B and −1.54 μ_B, respectively [38]. From the DFT calculations, Zhang et al. [63] reported that the total magnetic moment of $D0_3$-Mn_3Ga is highly dependent on the lattice constant. As the lattice constant increases, the covalent hybridization between the Ga and Mn atoms weakens, and thus the total magnetic moment increases. The change of lattice parameters has a profound effect on the local magnetic moment at the 4*b* sites. Kharel et al. [40] synthesized the cubic Mn_3Ga phase in the melt-spun ribbons with 25 at.% Ga, and demonstrated that this phase is antiferromagnetic, with a Néel temperature of 420 K and a zero magnetization at the room temperature. The discrepancy between the DFT calculations [37,38] and

experimental measurements [40] may come from the difference in the structure of the Mn_3Ga phase. In the melt-spun ribbons, the Mn_3Ga phase exhibits a disordered primitive cubic crystal structure [40], while in the DFT calculations, the Mn_3Ga phase adopts an ordered face-centered cubic crystal structure [37,38].

As shown in Fig. 13, both the Mn_2Ga(r) and Mn_3Ga_2 phases with the $L1_0$ structure are ferromagnetic. Bither and Cloud [64] used the magnetic measurements to determine the Curie temperature and the magnetic moment of the Mn_2Ga(r) phase to be 748 K and 0.502 μ_B/Mn, respectively. The Curie temperature and the magnetic moment of the Mn_3Ga_2 phase were measured to be 690 K and 1.5 μ_B/Mn by Tsuboya and Sugihara [65]. They reported a high coercivity for the Mn_3Ga_2 phase, which increases with the increase in the Mn content. The coercive force reaches 5.75 kOe in the alloy with 31.5 at.% Ga. Lu et al. [66] determined the Curie temperature of the Mn_3Ga_2 phase to be 650 K and the coercivity to be 4.18 kOe. Gourdon and Miller [45] proposed two possible magnetic structures for the ferromagnetic MnGa ($R\bar{3}m$) phase based on the DFT calculations. According to these two models, Ga will contribute to the total magnetic moment due to 3*d*-4*p* hybridization between the Mn and Ga electrons. Moreover, the Ga atoms that are surrounded by a larger number of Mn atoms have a larger local magnetic moment.

Sakuma [46] used the DFT calculations to predict the spin configuration in the $L1_0$-MnGa phase, and determined the magnetic moments for Mn and Ga to be 2.51 and −0.09 μ_B, respectively. They reported that the magnetic moments of Mn atoms are along the *c* axis, thus leading to a magnetocrystalline anisotropy of 2600 kJ/m^3. Yang et al. [47] studied the effect of strain on the magnetic structure of $L1_0$-MnGa using the DFT calculations. It was suggested that the magnetic moment for the unstrained phase is 2.51 μ_B/Mn, while that for the strained phase is 2.33 μ_B/Mn. That is because, owing to the strains, the decrease in the tetragonality (i.e., the decrease in the *c* value) of $L1_0$-MnGa will increase the hybridization between electrons and decrease the density of states at the Fermi level, thus decreasing the magnetic moment. Mix et al. [12] reported that as the Mn content increases, the Curie temperature and the anisotropy constant of $L1_0$-MnGa increase, while the maximum magnetization decreases. This work also studied the influence of processing methods on the magnetic properties of the $L1_0$-MnGa phase. The mechanical milling of the bulk samples will enhance the coercivity of the $L1_0$-MnGa phase, at the expense of the maximum magnetization. After hot compacting the mechanically milled powders, the $L1_0$-MnGa phase shows a high magnetization and a large coercivity.

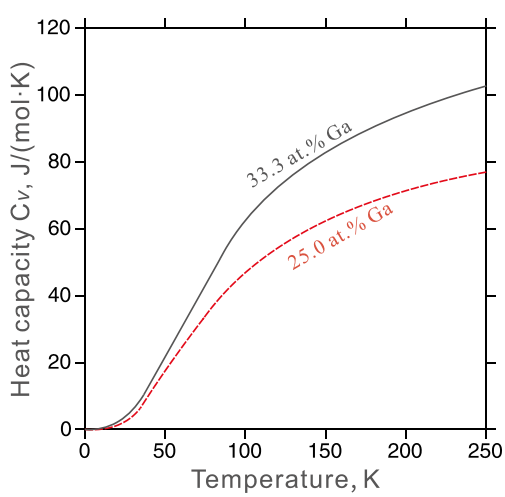

Fig. 14. Low-temperature heat capacity determined by experiments for two Mn–Ga alloys [34]. The black solid line is for Mn-33.3 at.% Ga alloy. The red dotted line is for Mn-25 at.% Ga alloy. (For interpretation of the references to colour in this figure legend, the reader is referred to the Web version of this article.)

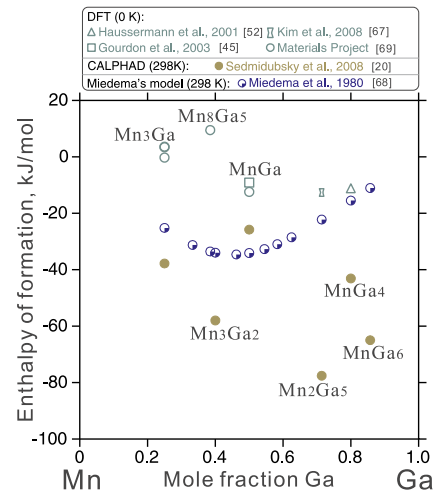

Fig. 15. Enthalpies of formation of the Mn–Ga intermetallic compounds calculated using the DFT [45,52,70,72], the CALPHAD method [20], and the Miedema model [71].

The magnetic properties of $L1_0$-MnGa can be readily tuned by altering the alloy composition due to its homogeneity range in this alloy system. Cui et al. [50] reported that the heat treatment, such as annealing, can enhance the degree of ordering of the $L1_0$ phase, thus contributing to the improvement of the coercivity. However, if the annealing temperature is too high, the grains become coarse, which will deteriorate the coercivity of the $L1_0$ phase. After annealing the powder containing 44 at.% Ga at 600 °C for 20 min, a coercivity as high as 6.2 kOe and a saturation magnetization of 61 emu/g can be reached.

Both $L1_0$ and $D0_{22}$ structures have a high Curie temperature as well as coercivity, and thus, they are suitable candidates for permanent magnets. Gong et al. [49] synthesized the $L1_0$ and $D0_{22}$ structures in melt-spun ribbons and suggested that the high coercivity of these two structures is due to the nucleation and pinning mechanisms, respectively. The magnetizations of these two structures are not comparable. Huh et al. [51] proposed that the magnetic properties of the $L1_0$-MnGa phase depend closely on the alloy composition. With the increase in the Mn content, the Curie temperature increases, while the magnetization and the anisotropy constant decrease. That is because, in the $L1_0$-MnGa phase, the magnetic moments of Mn align along the same direction, while the magnetic moments of Ga that have the opposite sign compared with those of Mn are so small that can be ignored. When excess Mn atoms are introduced, they will occupy the Ga sites, and align antiferromagnetically with other Mn atoms, causing a decrease in the magnetic anisotropy and the magnetization. Huh et al. [51] also reported that as the Mn content increases continuously, the ferromagnetic $L1_0$ phase finally transforms into the ferrimagnetic $D0_{22}$ phase, followed by a decrease in the magnetization.

The Mn_8Ga_5 phase was reported to be ferromagnetic, with a Curie temperature of 210 K, by Tsuboya and Sugihara [42]. Besides, the magnetic moment was determined to be 1.0 μ_B/Mn and 2.05 μ_B/Mn, based on the magnetization and the susceptibility measurements, respectively. Such a difference indicates that the magnetization of the alloy did not saturate under the applied magnetic field in the work of Tsuboya and Sugihara [42]. Tozman et al. [43] proposed that the Curie temperature and the magnetization of the Mn_8Ga_5 phase are influenced by the degree of atomic ordering, which can be altered by changing the annealing temperature and cooling rate.

Most Ga-rich phases are ferromagnetic, except for the Mn_5Ga_6 and Mn_5Ga_7 phases (see Fig. 13). Mn_3Ga_5 DQC approximant has a Curie temperature of 433 K [26]. The Curie temperature of the $MnGa_4$ phase was determined to be 453 K, based on the temperature dependence of the saturation magnetization [18]. The Curie temperature of the $MnGa_6$

phase is 420 K, according to Wachtel and Nier [17].

The ferromagnetic Mn_2Ga_5 phase was synthesized by Kitchingman and Norman [67,68] in an alloy with 73 at.% Ga. They determined the Curie temperature and the magnetic moment of the Mn_2Ga_5 phase to be 521 K and 1.777 μ_B/Mn, respectively, using the neutron diffraction. The possible spin configuration was also suggested in this study. Donishi et al. [69] synthesized the Mn_2Ga_5 phase in the vacuum evaporated thin films containing 70 at.% Ga, and successfully controlled the orientation of this phase by changing the annealing temperature. They demonstrated that a preferential alignment of the *c* axis perpendicular to the film surface can be achieved after annealing the amorphous film at 250 °C. Kim et al. [70] conducted the magnetic measurements, from which the Curie temperature and the magnetic moment of the Mn_2Ga_5 phase were determined to be 450 K and 1.355 μ_B/Mn, respectively. Besides, they performed the electronic band structure calculations to study the origin of such strong ferromagnetism. It was proposed that the super-degeneracy resulting from the bonding features between the atoms leads to the ferromagnetism for the Mn_2Ga_5 phase.

5. Thermochemical properties

So far, only limited studies have been performed about the thermochemical properties of the Mn–Ga system. Winterlik et al. [34] used the Quantum Design Physical Property Measurement System to obtain the low-temperature C_V (heat capacity at constant volume) for alloys containing 25.0 and 33.3 at.% Ga. This apparatus is commonly used for the determination of heat capacity at low temperatures, and the results are plotted in Fig. 14. Considering the negligible difference between C_V and C_P (heat capacity at constant pressure) at low temperatures, experimental data of C_V in Fig. 14 can be approximated to C_P and used in future CALPHAD-based thermodynamic modeling of the Mn–Ga system. As can be seen in Fig. 14, the C_V *vs.* T curve shows a typical metallic behavior, demonstrating major contributions from phonons within such a low-temperature range.

Fig. 15 presents the enthalpies of formation for the Mn–Ga intermetallic compounds, which were obtained using different methods. The Miedema model [71] was used to estimate the enthalpies of formation for all Mn–Ga intermetallic compounds listed in Table 4. The CALPHAD approach was used by Sedmidubský et al. [20] to assess the enthalpies of formation at room temperature for several Mn–Ga intermetallic compounds. Several researchers have calculated the total energy at 0 K for $MnGa_4$ [52], Mn_2Ga_5 [70], MnGa [45,72], Mn_8Ga_5 [72], and Mn_3Ga [72] phases, using the DFT calculations. The enthalpies of formation for the MnGa phase with the space group $P4/mmm$ ($L1_0$) and $R\bar{3}m$ are −12.447 [72] and −9.167 kJ/mol [45], respectively. For the Mn_3Ga phase, the enthalpies of formation for the $D0_{22}$, $D0_{19}$, and $D0_3$ structures are −0.289, 3.570, and 3.377 kJ/mol [72], respectively. Therefore, from the DFT calculations, the most stable structure for the MnGa phase is $L1_0$, and that for the Mn_3Ga phase is $D0_{22}$. This is contradictory to the experimental results, which demonstrated that the MnGa phase with space group $R\bar{3}m$ and the Mn_3Ga phase with the $D0_{19}$-type structure are more stable. According to the DFT calculations, the enthalpy of formation for the Mn_8Ga_5 phase with the Cu_5Zn_8-type structure is 9.456 kJ/mol [72], which suggests this structure is metastable. Therefore, the stable structure for the Mn_8Ga_5 phase should be the Al_4Cu_9-type, as determined by Minakuchi et al. [19]. However, this assumption needs to be validated by further studies. Meanwhile, as shown in Fig. 15, there is a large discrepancy between formation energies calculated by CALPHAD-based thermodynamic descriptions and by DFT. As mentioned earlier, the work of Sedmidubský et al. [20] involved many simplifications and cannot lead to reliable thermodynamic calculations. Therefore, their reported formation energies deviate largely from those calculated by DFT. A self-consistent CALPHAD-based thermodynamic assessment of the Mn–Ga system is ongoing and will be published later.

6. Conclusions

Despite the scientific and technological importance of Mn-Ga-based alloys, reports related to thermodynamics of the Mn–Ga system are still limited and exhibit great discrepancies. Therefore, this work comprehensively reviews current progress on studies of the phase diagram, crystallography, magnetism, and thermochemical properties for this binary system. Afterward, a new version of the Mn–Ga phase diagram, which incorporates relatively reliable results from two groups, is recommended. The information about crystal structure, magnetic transition temperature, magnetic moment, heat capacity, and enthalpy of formation for Mn–Ga intermetallic compounds is summarized. This work provides guidelines for future investigations of the Mn–Ga system, and the summarized information can serve as useful inputs for future thermodynamic modeling.

Based on critical evaluations, a considerable amount of work is still required to have a better understanding of the thermodynamics of the Mn–Ga system. For example, experimental studies about phase equilibria on the Mn-rich side are highly suggested to clarify existing discrepancies among works performed by different researchers. A self-consistent CALPHAD-based database should be established to facilitate alloy and processing designs of Mn–Ga based materials. Thermochemical properties, such as activity, enthalpy of mixing of liquid as well as solid solutions, and heat capacities covering more compositions, also deserve further experimental determination, to better support thermodynamic modeling. DFT calculations should be performed to obtain the local magnetic moment for intermetallic compounds, which can lead to a more physically sound description of the magnetic phase diagram. Enthalpies of formation for intermetallic compounds and different structures of Mn_3Ga, Mn_8Ga_5, and MnGa phases need to be calculated using DFT, to evaluate the phase stability better.

Declaration of competing interest

The authors declare that they have no known competing financial interests or personal relationships that could have appeared to influence the work reported in this paper.

Acknowledgments

The authors are grateful for helpful discussions with Dr. Soumya Sridar, Dr. Biao Hu, and Prof. Markus Chmielus at the University of Pittsburgh. W.X. acknowledges funding from the National Science Foundation under award DMR - 1808082, and from the University of Pittsburgh, through the Central Research Development Fund (CRDF). The authors would like to dedicate this work to Prof. Em. Gerhard Inden's 80th birthday.

References

[1] M. Pasquale, Mechanical sensors and actuators, Sensors Actuators, A Phys. 106 (2003) 142–148, https://doi.org/10.1016/S0924-4247(03)00153-5.
[2] K. Ullakko, J.K. Huang, V.V. Kokorin, R.C. O'Handley, Magnetically controlled shape memory effect in Ni_2MnGa intermetallics, Scr. Mater. 36 (1997) 1133–1138, https://doi.org/10.1016/S1359-6462(96)00483-6.
[3] L. Pareti, M. Solzi, F. Albertini, A. Paoluzi, Giant entropy change at the co-occurrence of structural and magnetic transitions in the $Ni_{2.19}Mn_{0.81}Ga$ Heusler alloy, Eur. Phys. J. B. 32 (2003) 303–307, https://doi.org/10.1140/epjb/e2003-00102-y.
[4] V.D. Buchelnikov, V.V. Sokolovskiy, Magnetocaloric effect in Ni-Mn-X (X = Ga, In, Sn, Sb) heusler alloys, Phys. Met. Metallogr. 112 (2011) 633–665, https://doi.org/10.1134/S0031918X11070052.
[5] M. Tanaka, J.P. Harbison, T. Sands, B. Philips, T.L. Cheeks, J. De Boeck, L.T. Florez, V.G. Keramidas, Epitaxial MnGa/NiGa magnetic multilayers on GaAs, Appl. Phys. Lett. 63 (1993) 696–698, https://doi.org/10.1063/1.109932.
[6] K. Wang, A. Chinchore, W. Lin, D.C. Ingram, A.R. Smith, A.J. Hauser, F. Yang, Epitaxial growth of ferromagnetic δ-phase manganese gallium on semiconducting scandium nitride (0 0 1), J. Cryst. Growth 311 (2009) 2265–2268, https://doi.org/10.1016/j.jcrysgro.2009.02.033.

[7] A. Grunebohm, H.C. Herper, M.E. Gruner, P. Entel, Suitability of Fe/GaAs and (Co, Ni)Mn(Ga,Ge) for spintronics applications: an Ab initio study, IEEE Trans. Magn. 45 (2009) 3965–3968, https://doi.org/10.1109/TMAG.2009.2022409.

[8] B. Dieny, V.S. Speriosu, S.S.P. Parkin, B.A. Gurney, D.R. Wilhoit, D. Mauri, Giant magnetoresistive in soft ferromagnetic multilayers, Phys. Rev. B. 43 (1991) 1297–1300, https://doi.org/10.1103/PhysRevB.43.1297.

[9] H. Kurt, K. Rode, H. Tokuc, P. Stamenov, M. Venkatesan, J.M.D. Coey, Exchange-biased magnetic tunnel junctions with antiferromagnetic-Mn_3Ga, Appl. Phys. Lett. 101 (2012) 3–7, https://doi.org/10.1063/1.4768941.

[10] L. Zhu, S. Nie, K. Meng, D. Pan, J. Zhao, H. Zheng, Multifunctional $L1_0$-$Mn_{1.5}Ga$ films with ultrahigh coercivity, giant perpendicular magnetocrystalline anisotropy and large magnetic energy product, Adv. Mater. 24 (2012) 4547–4551, https://doi.org/10.1002/adma.201200805.

[11] J.M.D. Coey, New permanent magnets; Manganese compounds, J. Phys. Condens. Matter 26 (2014), https://doi.org/10.1088/0953-8984/26/6/064211.

[12] T. Mix, K.H. Müller, L. Schultz, T.G. Woodcock, Formation and magnetic properties of the $L1_0$ phase in bulk, powder and hot compacted Mn-Ga alloys, J. Magn. Magn. Mater. 391 (2015) 89–95, https://doi.org/10.1016/j.jmmm.2015.04.097.

[13] B. Balke, G.H. Fecher, J. Winterlik, C. Felser, Mn_3Ga, a compensated ferrimagnet with high Curie temperature and low magnetic moment for spin torque transfer applications, Appl. Phys. Lett. 90 (2007) 1–3, https://doi.org/10.1063/1.2722206.

[14] J. Winterlik, S. Chadov, A. Gupta, V. Alijani, T. Gasi, K. Filsinger, B. Balke, G. H. Fecher, C.A. Jenkins, F. Casper, J. Kübler, G.D. Liu, L. Gao, S.S.P. Parkin, C. Felser, Design scheme of new tetragonal heusler compounds for spin-transfer torque applications and its experimental realization, Adv. Mater. 24 (2012) 6283–6287, https://doi.org/10.1002/adma.201201879.

[15] R.M. Gutiérrez-Pérez, J.T. Holguín-Momaca, J.T. Elizalde-Galindo, F. Espinosa-Magaña, S.F. Olive-Méndez, Giant magnetization on Mn_3Ga ultra-thin films grown by magnetron sputtering on SiO_2/Si(001), J. Appl. Phys. 117 (2015), https://doi.org/10.1063/1.4916158.

[16] H.G. Meissner, K. Schubert, T.R. Anantharaman, The constitution and structure of Manganese-Gallium alloys, Proc. Indiana Acad. Sci. A. 61 (1965) 340–366, https://doi.org/10.1007/BF03049257.

[17] E. Wachtel, K.J. Nier, Magnetic investigation of the systems Manganese-Gallium in solid and liquid states (in German), Z.Metallkunde. 56 (1965) 779–789.

[18] X.S. Lu, J.K. Liang, T.J. Shi, M.G. Zhou, A X-ray investigation of the Manganese-Gallium system (in Chinese), Acta Phys. Sin. 29 (1980) 469–484.

[19] K. Minakuchi, R.Y. Umetsu, K. Ishida, R. Kainuma, Phase equilibria in the Mn-rich portion of Mn-Ga binary system, J. Alloy. Comp. 537 (2012) 332–337, https://doi.org/10.1016/j.jallcom.2012.04.065.

[20] D. Sedmidubský, J. Leitner, Z. Sofer, Phase relations in the Ga-Mn-N system, J. Alloy. Comp. 452 (2008) 105–109, https://doi.org/10.1016/j.jallcom.2006.11.212.

[21] H. Okamoto, Phase Diagrams for Binary Alloys, second ed., ASM International, Ohio, 2010.

[22] T.B. Massalski, H. Okamoto, Binary Alloy Phase Diagrams, second ed., ASM International, Ohio, 1990.

[23] H. Masumoto, K. Watanabe, M. Mitera, Equilibrium diagram of Mn-Ga binary alloys, Trans. Jpn. Inst. Met. 19 (1978) 395–399, https://doi.org/10.2320/matertrans1960.19.395.

[24] M. Tillard, C. Belin, Investigation in the Ga-rich side of the Mn-Ga system: synthesis and crystal structure of $MnGa_4$ and $MnGa_{5-x}$ (x ~ 0.15), Intermetallics 29 (2012) 147–154, https://doi.org/10.1016/j.intermet.2012.05.011.

[25] H. Okamoto, Supplemental literature review of binary phase diagrams: Ag-Sn, Al-Pd, Ba-Gd, Ba-Pr, Cu-P, Dy-Ni, Ga-Mn, Gd-Sb, Gd-Zr, Ho-Te, Lu-Sb, and Mn-Nb, J. Phase Equilibria Diffusion 35 (2014) 105–116, https://doi.org/10.1007/s11669-013-0262-x.

[26] J.S. Wu, K.H. Kuo, Decagonal quasicrystal and related crystalline phases in Mn-Ga alloys with 52 to 63 a/o Ga, Metall. Mater. Trans. A Phys. Metall. Mater. Sci. 28 (1997) 729–742, https://doi.org/10.1007/s11661-997-1000-y.

[27] J.S. Wu, X.Z. Li, K.H. Kuo, A high-resolution electron microscopy study of the structure of the (1/0, 2/1) and (1/1, 1/1) decagonal approximants in Ga_6Mn_5, Philos. Mag. Lett. 77 (1998) 359–370, https://doi.org/10.1080/095008398178345.

[28] K. Schubert, T.R. Anantharaman, H.O.K. Ata, H.G. Meissner, M. Pötzschke, W. Rossteutscher, E. Stolz, Einige strukturelle Ergebniss an metallischen phasen (6) (in German), Naturwissenschaften 47 (1960) 512, https://doi.org/10.1007/BF00641115.

[29] I. Tsuboya, M. Sugihara, Magnetic properties of ε phase in Mn-Ga system, J. Phys. Soc. Jpn. 18 (1963) 143, https://doi.org/10.1143/JPSJ.18.143.

[30] E.K.G. Kádár, Neutron diffraction study of Mn_3Ga, Solid State Commun. 8 (1970) 1653–1655, https://doi.org/10.1016/0038-1098(70)90484-9.

[31] H. Niida, T. Hori, Y. Nakagawa, Magnetic properties and crystal distortion of hexagonal Mn_3Ga, J. Phys. Soc. Jpn. 52 (1983) 1512–1514.

[32] H. Niida, T. Hori, Y. Nakagawa, Magnetic properties of ε-MnGa alloys with the DO_{19} type structure, J. Phys. Colloq. 49 (1988), https://doi.org/10.1051/jphyscol:1988873. C8-C173-C8-174.

[33] J.N. Feng, X.G. Zhao, X.K. Ning, C.W. Shih, W.C. Chang, S. Ma, W. Liu, Z.D. Zhang, Phase evaluation, magnetic, and electric properties of $Mn_{60+x}Ga_{40-x}$ (x=0-15) ribbons, J. Appl. Phys. 115 (2014) 15–17, https://doi.org/10.1063/1.4868081.

[34] J. Winterlik, B. Balke, G.H. Fecher, C. Felser, M.C.M. Alves, F. Bernardi, J. Morais, Structural, electronic, and magnetic properties of tetragonal $Mn_{3-x}Ga$: experiments and first-principles calculations, Phys. Rev. B Condens. Matter Mater. Phys. 77 (2008) 1–12, https://doi.org/10.1103/PhysRevB.77.054406.

[35] H. Masumoto, K. Watanabe, M. Mitera, On the DO_{22}-type alloys in the Mn-Ga system and their magnetic properties (in Japanese), Nippon Kinzoku Gakkaishi 42 (1978) 474–479.

[36] H. Niida, T. Hori, H. Onodera, Y. Yamaguchi, Y. Nakagawa, Magnetization and coercivity of $Mn_{3-\delta}Ga$ alloys with a $D0_{22}$-type structure, J. Appl. Phys. 79 (1996) 5946, https://doi.org/10.1063/1.362115.

[37] J. Kübler, Ab initio estimates of the Curie temperature for magnetic compounds, J. Phys. Condens. Matter 18 (2006) 9795–9807, https://doi.org/10.1088/0953-8984/18/43/003.

[38] S. Wurmehl, H.C. Kandpal, G.H. Fecher, C. Felser, Valence electron rules for prediction of half-metallic compensated-ferrimagnetic behaviour of Heusler compounds with complete spin polarization, J. Phys. Condens. Matter 18 (2006) 6171–6181, https://doi.org/10.1088/0953-8984/18/27/001.

[39] Y. Huh, P. Kharel, V.R. Shah, E. Krage, R. Skomski, J.E. Shield, D.J. Sellmyer, Magnetic and structural properties of rapidly quenched tetragonal $Mn_{3-x}Ga$ nanostructures, IEEE Trans. Magn. 49 (2013) 3277–3280, https://doi.org/10.1109/TMAG.2013.2244856.

[40] P. Kharel, Y. Huh, N. Al-Aqtash, V.R. Shah, R.F. Sabirianov, R. Skomski, D. J. Sellmyer, Structural and magnetic transitions in cubic Mn_3Ga, J. Phys. Condens. Matter 26 (2014), https://doi.org/10.1088/0953-8984/26/12/126001.

[41] D. Zhang, B. Yan, S.C. Wu, J. Kübler, G. Kreiner, S.S.P. Parkin, C. Felser, First-principles study of the structural stability of cubic, tetragonal and hexagonal phases in Mn_3Z (Z=Ga, Sn and Ge) Heusler compounds, J. Phys. Condens. Matter 25 (2013) 1–6, https://doi.org/10.1088/0953-8984/25/20/206006.

[42] I. Tsuboya, M. Sugihara, Magnetic properties of ζ phase in Mn-Ga system, J. Phys. Soc. Jpn. 18 (1963) 1096.

[43] P. Tozman, J.M.D. Coey, Z. Gercsi, Structure and magnetic order in Mn_8Ga_5, Acta Mater. 113 (2016) 147–154, https://doi.org/10.1016/j.actamat.2016.04.053.

[44] T. Saito, R. Nishimura, Hard magnetic properties of Mn-Ga melt-spun ribbons, J. Appl. Phys. 112 (2012) 50–53, https://doi.org/10.1063/1.4759351.

[45] O. Gourdon, G.J. Miller, Reinvestigation of the GaMn structure and theoretical studies of its electronic and magnetic properties, J. Solid State Chem. 173 (2003) 137–147, https://doi.org/10.1016/S0022-4596(02)00031-2.

[46] A. Sakuma, Electronic structures and magnetism of CuAu-type MnNi and MnGa, J. Magn. Magn. Mater. 187 (1998) 105–112, https://doi.org/10.1016/0304-8853(94)01149-4.

[47] Z.X. Yang, J. Li, D.S. Wang, K.M. Zhang, X.D. Xie, Electronic structure and magnetic properties of δ-MnGa, J. Magn. Magn. Mater. 182 (1998) 369–374, https://doi.org/10.1016/S0304-8853(97)01029-9.

[48] E. Lu, D.C. Ingram, A.R. Smith, J.W. Knepper, F.Y. Yang, Reconstruction control of magnetic properties during epitaxial growth of ferromagnetic $Mn_{3-\delta}Ga$ on wurtzite GaN(0001), Phys. Rev. Lett. 97 (2006) 1–4, https://doi.org/10.1103/PhysRevLett.97.146101.

[49] W. Gong, X. Zhao, W. Fan, J. Feng, A. Lin, J. He, W. Liu, Z. Zhang, Structure, magnetic properties, and coercivity mechanism of rapidly quenched Mn_xGa ribbons, IEEE Trans. Magn. 51 (2015) 10–13, https://doi.org/10.1109/TMAG.2015.2434936.

[50] B.Z. Cui, M. Marinescu, J.F. Liu, Ferromagnetic tetragonal $L1_0$-Type MnGa isotropic nanocrystalline microparticles, IEEE Trans. Magn. 49 (2013) 3322–3325, https://doi.org/10.1109/TMAG.2013.2245868.

[51] Y. Huh, P. Kharel, V.R. Shah, X.Z. Li, R. Skomski, D.J. Sellmyer, Magnetism and electron transport of Mn_yGa ($1<y<2$) nanostructures, J. Appl. Phys. 114 (2013) 2–6, https://doi.org/10.1063/1.4812561.

[52] U. Häussermann, P. Viklund, M. Boström, R. Norrestam, S.I. Simak, Bonding and physical properties of Hume-Rothery compounds with the $PtHg_4$ structure, Phys. Rev. B Condens. Matter Mater. Phys. 63 (2001) 1–10, https://doi.org/10.1103/PhysRevB.63.125118.

[53] J.S. Wu, S.P. GE, K.H. Kuo, A new orthorhombic approximant of the Ga-Mn and Ga-Fe-Cu-Si decagonal quasicrystals consisting entirely of uniformly oriented 'crown' subunits, Philos. Mag. A 79 (1999) 1787–1803, https://doi.org/10.1080/01418619908210392.

[54] J.S. Wu, K.H. Kuo, A structural model of the orthorhombic Ga_7Mn_5 derived from its HREM image, Micron 31 (2000) 459–467, https://doi.org/10.1016/S0968-4328(99)00125-0.

[55] M. Boström, S. Hovmöller, Preparation and crystal structure of the pseudo-decagonal approximant Mn_3Ga_5, J. Solid State Chem. 153 (2000) 398–403, https://doi.org/10.1006/jssc.2000.8790.

[56] M. Uchida, Y. Matsui, A new stacking motif in the decagonal approximant Mn_3Ga_5, Philos. Mag. Lett. 81 (2001) 667–671, https://doi.org/10.1080/09500830110062816.

[57] M. Boström, S. Hovmöller, Preparation and crystal structure of the novel decagonal approximant $Mn_{123}Ga_{137}$, J. Alloy. Comp. 314 (2001) 154–159, https://doi.org/10.1016/S0925-8388(00)01259-7.

[58] W. Xiong, H. Zhang, L. Vitos, M. Selleby, Magnetic phase diagram of the Fe-Ni system, Acta Mater. 59 (2011) 521–530, https://doi.org/10.1016/j.actamat.2010.09.055.

[59] W. Xiong, P. Hedström, M. Selleby, J. Odqvist, M. Thuvander, Q. Chen, An improved thermodynamic modeling of the FeCr system down to zero kelvin coupled with key experiments, Calphad Comput. Coupling Phase Diagrams Thermochem. 35 (2011) 355–366, https://doi.org/10.1016/j.calphad.2011.05.002.

[60] W. Xiong, M. Selleby, Q. Chen, J. Odqvist, Y. Du, Phase equilibria and thermodynamic properties in the Fe-Cr system, Crit. Rev. Solid State Mater. Sci. 35 (2010) 125–152, https://doi.org/10.1080/10408431003788472.

[61] W. Xiong, Q. Chen, P.A. Korzhavyi, M. Selleby, An improved magnetic model for thermodynamic modeling, Calphad Comput. Coupling Phase Diagrams Thermochem. 39 (2012) 11–20, https://doi.org/10.1016/j.calphad.2012.07.002.
[62] J.Z. Wei, R. Wu, Y.B. Yang, X.G. Chen, Y.H. Xia, Y.C. Yang, C.S. Wang, J.B. Yang, Structural properties and large coercivity of bulk $Mn_{3-x}Ga$ ($0 \leq x \leq 1.15$), J. Appl. Phys. 115 (2014) 15–17, https://doi.org/10.1063/1.4866844.
[63] H. Zhang, W. Liu, T. Lin, W. Wang, G. Liu, Phase stability and magnetic properties of Mn_3Z (Z = Al, Ga, In, Tl, Ge, Sn, Pb) Heusler alloys, Appl. Sci. 9 (2019), https://doi.org/10.3390/app9050964.
[64] T.A. Bither, W.H. Cloud, Magnetic tetragonal δ phase in the Mn-Ga binary, J. Appl. Phys. 36 (1965) 1501–1502, https://doi.org/10.1063/1.1714349.
[65] I. Tsuboya, M. Sugihara, Magnetic properties of Mn-Ga alloys with a high coercive force, J. Phys. Soc. Jpn. 20 (1965) 170, https://doi.org/10.1143/JPSJ.20.170.
[66] Q.M. Lu, F. Yu, M. Yue, H.G. Zhang, Y.Q. Li, X.L. Yan, Y.Q. Liu, J.X. Zhang, Phase structure and magnetic properties of Mn_3Ga_2 alloy, J. Appl. Phys. 115 (2014) 2–4, https://doi.org/10.1063/1.4868080.
[67] W.J. Kitchingman, P.L. Norman, X-ray diffraction studies of the ternary alloys $(V, Mn)_2Ga_5$, Acta Crystallogr. Sect. B Struct. Crystallogr. Cryst. Chem. 28 (1972) 1311–1312, https://doi.org/10.1107/s0567740872004169.
[68] W.J. Kitchingman, P.L. Norman, Neutron diffraction, magnetic and superconducting measurements on vanadium–manganese–gallium alloys, J. Appl. Crystallogr. 6 (1973) 240–243, https://doi.org/10.1107/s002188987300854x.
[69] K. Donishi, K. Morii, Y. Nakayama, Formation of Mn_2Ga_5 phase in amorphous $Mn_{30}Ga_{70}$ thin films, Mater. Trans. 30 (1989) 455–458, https://doi.org/10.2320/matertrans1989.30.455.
[70] S.H. Kim, M. Boström, D.K. Seo, Two-dimensional superdegeneracy and structure-magnetism correlations in strong ferromagnet, Mn_2Ga_5, J. Am. Chem. Soc. 130 (2008) 1384–1391, https://doi.org/10.1021/ja0765924.
[71] A.R. Miedema, P.F. de Châtel, F.R. de Boer, Cohesion in alloys - fundamentals of a semi-empirical model, Phys. B+C 100 (1980) 1–28, https://doi.org/10.1016/0378-4363(80)90054-6.
[72] Materials project. https://materialsproject.org/.
[73] K. Schubert, H.G. Meissner, M. Pötzschke, W. Rossteutscher, E. Stolz, Einige strukturdaten metallischer phasen (7) (in German), Naturwissenschaften 3 (1962) 57, https://doi.org/10.1007/BF00595382.
[74] K. Schubert, H.G. Meissner, A. Raman, W. Rossteutscher, Einige strukturdaten metallischer phasen (9) (in German), Naturwissenschaften 12 (1964) 287, https://doi.org/10.1007/BF00625465.
[75] M. Hasegawa, I. Tsuboya, Magnetic properties of η phase in Mn-Ga system, J. Phys. Soc. Jpn. 20 (1965) 464, https://doi.org/10.1143/JPSJ.20.464.
[76] X.S. Lu, J.K. Liang, R.Z. Yang, The crystal structure of MnGa and the degree of order (in Chinese), Acta Phys. Sin. 28 (1979) 54–61.
[77] K.H.J. Buschow, P.G. Van Engen, R. Jongebreur, Magneto-optical properties of metallic ferromagnetic materials, J. Magn. Magn. Mater. 38 (1983) 1–22, https://doi.org/10.1016/0304-8853(83)90097-5.
[78] K. Rode, N. Baadji, D. Betto, Y.C. Lau, H. Kurt, M. Venkatesan, P. Stamenov, S. Sanvito, J.M.D. Coey, E. Fonda, E. Otero, F. Choueikani, P. Ohresser, F. Porcher, G. André, Site-specific order and magnetism in tetragonal Mn_3Ga thin films, Phys. Rev. B Condens. Matter Mater. Phys. 87 (2013) 1–14, https://doi.org/10.1103/PhysRevB.87.184429.
[79] A.A. El-Gendy, G. Hadjipanayis, Nanostructured $D0_{22}$-Mn_3Ga with high coercivity, J. Phys. D Appl. Phys. 48 (2015) 1–4, https://doi.org/10.1088/0022-3727/48/12/125001.
[80] P. Villars, L.D. Calvert, Pearson's Handbook of Crystallographic Data for Intermetallic Phases, second ed., ASM International, Ohio, 1991.